Reduced description of exact coherent states in parallel shear flows

Cédric Beaume, Gregory P. Chini, Keith Julien, and Edgar Knobloch

Phys. Rev. E **91**, 043010 — Published 15 April 2015

DOI: 10.1103/PhysRevE.91.043010

Reduced description of exact coherent states in parallel shear flows

Cédric Beaume*
Department of Aeronautics, Imperial College London, London SW7 2AZ, UK

Greg P. Chini†
Department of Mechanical Engineering & Program in Integrated Applied Mathematics, University of New Hampshire, Durham NH 03824

Keith Julien‡
Department of Applied Mathematics, University of Colorado at Boulder, Boulder CO 80309

Edgar Knobloch§
Department of Physics, University of California, Berkeley CA 94720, USA

A reduced description of exact coherent structures in the transition regime of plane parallel shear flows is developed, based on the Reynolds number scaling of streamwise-averaged (mean) and streamwise-varying (fluctuation) velocities observed in numerical simulations. The resulting system is characterized by an effective unit Reynolds number mean equation coupled to linear equations for the fluctuations, regularized by formally higher-order diffusion. Stationary coherent states are computed by solving the resulting equations simultaneously using a robust numerical algorithm developed for this purpose. The algorithm determines self-consistently the amplitude of the fluctuations for which the associated mean flow is just such that the fluctuations neither grow nor decay. The procedure is used to compute exact coherent states of a flow introduced by P. G. Drazin & W. H. Reid (*Hydrodynamic Stability*, Cambridge University Press (1981)) and studied by F. Waleffe (Phys. Fluids **9**, 883 (1997)): a linearly stable, plane parallel shear flow confined between stationary stress-free walls and driven by a sinusoidal body force. Numerical continuation of the lower branch states to lower Reynolds numbers reveals the presence of a saddle-node; the saddle-node allows access to upper branch states that, like the lower branch states, appear to be self-consistently described by the reduced equations. Both lower and upper branch states are characterized in detail.

* ced.beaume@gmail.com
† greg.chini@unh.edu
‡ keith.julien@colorado.edu
§ knobloch@berkeley.edu

I. INTRODUCTION

Exact, fully nonlinear, three-dimensional (3D) solutions of the Navier-Stokes equations play an important role in our understanding of the transition to turbulence in parallel shear flows and of the recurrence properties of the turbulence that results. These solutions, first computed by Nagata [1] and Waleffe [2] and now called *exact coherent states* (ECS), may take the form of time-independent states (i.e., equilibria) or time-periodic states (e.g., traveling waves). ECS have now been computed by numerous investigators for a number of different flows, including plane Couette flow [3] and pipe flow [4–7]. Typically, these solutions consist of streamwise-oriented streaks and vortices that bear a striking qualitative and even quantitative resemblance to the coherent structures commonly observed in turbulent wall flows, although they are generally unstable. In fact, despite their instability, ECS are frequently observed as transients in both shear flow simulations and experiments. Analysis of a low-order model by Waleffe [2] and a more systematic numerical study by Schmiegel [8] reveal that the ECS in plane Couette flow (PCF) are born in a saddle-node bifurcation as the Reynolds number Re increases, and continue as upper- and lower-branch solutions; this ECS bifurcation scenario seems generic in that it is commonly found in other shear flows. Much of the interest in ECS can be attributed to the possibility that upper-branch solutions comprise the "skeleton" of a high-dimensional "turbulent" attractor in the shear-flow phase space. Both Waleffe [9] and Kawahara & Kida [10] demonstrate that certain low-order statistics of PCF turbulence, particularly the mean and root-mean-square (rms) velocity profiles, can be accurately reproduced using these unstable solutions, quantitatively attesting to their physical relevance.

In two particularly insightful papers, Waleffe [2, 9] identifies a fully nonlinear process, involving the interaction of streamwise-oriented streaks and rolls, that sustains lower-branch ECS in plane parallel shear flows (including PCF), following earlier work by Hall & Smith [11] on the closely related phenomenon of vortex-wave interaction. Certain lower branch solutions have the remarkable property that they have only a *single* unstable eigendirection. These coherent states appear to separate, in phase space, disturbances that decay, causing relaminarization of the flow, from those that follow an excursion toward a turbulent (or at least transiently chaotic) state. For this reason, investigation of these "edge states" and their stability is of great interest, offering tantalizing opportunities for flow control. Importantly, the recent discovery by Schneider *et al.* [12] of spatially localized edge states in PCF has served to further increase interest in ECS by establishing that they are not special solutions found only in small laterally-periodic domains but, rather, that they exist in unbounded flows and may thus play a role in transition in open shear flows.

In general, the extraction of both lower and upper branch ECS in PCF, as in other shear flows, has required substantial computational effort. In particular, because ECS are typically disconnected from the structureless base shear flow, standard methods based on linear theory cannot be used to identify them, and more sophisticated algorithms (or considerable ingenuity and physical intuition – see [2, 9]) are required. These challenges are exacerbated for flows at large Reynolds numbers and in large domains. To alleviate these challenges we propose in this paper a reduced description of ECS in the transition regime. Our approach,

Mode	u_0	(v_0, w_0)	(u_1, v_1, w_1)	(u_2, v_2, w_2)	(u_3, v_3, w_3)	(u_n, v_n, w_n)
Scaling	$O(1)$	$O(\mathrm{Re}^{-1})$	$O(\mathrm{Re}^{-0.9})$	$O(\mathrm{Re}^{-1.6})$	$O(\mathrm{Re}^{-2.2})$	$o(\mathrm{Re}^{-2.2})$

TABLE I. Summary of the scalings obtained by Wang *et al.* [16] for lower branch ECS in plane Couette flow. These authors decompose the ECS into streamwise Fourier modes: $\mathbf{u}(x, y, z, t) = y\hat{\mathbf{x}} + \sum_{n=-N/2}^{N/2} \mathbf{u_n}(y, z)e^{in\theta} + c.c.$, where n denotes the index of the Fourier mode $\mathbf{u_n}$, N is the number of Fourier modes retained and $\theta = \alpha(x - ct)$. Here α is the fundamental streamwise wave number, c is the speed of the wave (in the case of a traveling wave solution), and *c.c.* denotes the complex conjugate. The last column shows that higher harmonics ($n > 3$) decay faster than the primary ones.

like the related approach of Hall & Sherwin [13] and Blackburn *et al.* [14], is based on a decomposition of the flow into streamwise-invariant (i.e., mean) and streamwise-varying (i.e., fluctuation, or "wave") components and subsequent exploitation of the properties of these fields as observed in numerical simulations. Specifically, we use the fact that along the lower ECS branch streamwise-invariant streaks are $O(1)$ as $\mathrm{Re} \to \infty$ while the streamwise-invariant rolls scale as $O(\mathrm{Re}^{-1})$, as originally suggested by [15] and confirmed by Wang *et al.* [16] for PCF. Fundamental streamwise-varying modes also scale roughly as $O(\mathrm{Re}^{-1})$ – Wang *et al.* [16] cite an exponent of approximately -0.9 – but higher harmonics are found to be $o(\mathrm{Re}^{-1})$, see table I. We note that Hall & Sherwin [13] have used the appropriate critical layer scalings suggested by Hall & Smith [11] to develop an asymptotic analysis valid in the limit $\mathrm{Re} \to \infty$. The resulting theory leads to a two-dimensional (2D) system for the streamwise-averaged fields at *unit* rescaled Reynolds number coupled to a quasi-linear inviscid eigenvalue problem for *neutral* disturbances to a mean streaky streamwise (x-directed) flow $u_0(y, z)$, where y and z are wall-normal and spanwise coordinates, respectively. This eigenvalue problem is singular, possessing a non-planar critical layer at $u_0(y, z) = 0$. The authors perform a careful matched asymptotic analysis to incorporate a viscously regularized critical layer, ultimately deriving jump conditions across the layer that link the mean fields on either side. In addition to reducing the computational cost of numerically solving for the lower-branch ECS at large Re, their analysis clearly demonstrates the physical mechanism by which the fluctuations sustain the mean fields in this limit: namely, steady streaming is driven within the critical layer, which in turn drives the mean flow outside the layer. Despite this Hall & Sherwin [13] are obliged to employ a sophisticated high-order domain-decomposition numerical scheme to solve their equations, which requires the numerical grid to be adaptively updated since the location of the critical layer is not known *a priori*.

For all its merit the asymptotic analysis of Hall & Sherwin [13] generates solutions whose dynamical significance remains to be established since at extreme values of the Reynolds number the flow is likely to be fully turbulent. In contrast, our primary interest is in transitional and low Re turbulent flows, for which the dynamical relevance of the ECS is, in fact, clear [3]. At these more moderate values of the Reynolds number (yet still large compared to unity), the critical layer broadens into a critical *region*. Consequently we seek a uniform approximation over the entire domain. To obtain a uniformly valid system, we

retain formally small dissipation terms in the fluctuation equations, as described by Beaume [17] and subsequently employed by Blackburn *et al.* [14]. This procedure obviates the need for explicit introduction and subsequent smoothing of jump conditions and for any further regularization of the fluctuation equations. Since jump conditions are not imposed, there is no need for adaptive mesh refinement associated with dynamic tracking of the critical layer. Of course, for very large Re sufficiently many modes or grid points must still be used to resolve the inevitable sharp gradient regions that arise. This issue is mitigated, however, in the transition regime.

Since we are interested in *equilibrium* ECS we choose a simple body-forced parallel shear flow first proposed by Drazin and Reid [18] and later studied by Waleffe [2], which we refer to as "Waleffe flow" (hereafter WF, see Sec. II). This flow is a close relative of PCF, being linearly stable for all Re, implying a likely connection between the ECS we compute and those found by Nagata [1], Clever & Busse [19] and later continued via homotopy by Waleffe [20] to other flows. Our reasons for studying this flow instead of plane Couette flow are threefold: (a) the properties of the ECS in this flow have not been studied, (b) trigonometric basis functions may be employed in *both* the wall-normal and spanwise directions to provide a higher mesh density within the critical region, and (c) it provides an excellent example of a nontrivial configuration on which the new algorithm can be tested. In particular, we employ – and, as necessary, refine – an *equispaced* grid in both coordinate directions, and as a result are able to identify structures not only in the direction normal to the broadened critical layer but also *along* it. Finally, and somewhat remarkably, we demonstrate in Sec. IV that our asymptotically-reduced PDE model admits both lower branch and *upper branch* solutions [21]: in spite of the large Reynolds number scaling incorporated into the theory, the approach proves sufficiently robust to capture the saddle node bifurcation at which both the lower and upper branch ECS are born. Thus, our reduced PDEs should prove useful for a variety of further studies of parallel shear flows that aim, for example, to investigate streamwise and spanwise localization.

The remainder of this paper is organised as follows. In Sec. II we describe in detail the multiscale averaging approach we use to obtain our reduced description. Sec. III outlines the customized numerical algorithm we develop to solve the reduced equations while Sec. IV summarizes the results obtained. The paper ends with brief conclusions in Sec. V.

II. MULTISCALE SYSTEM

Incompressible channel flow driven by a volume force $\mathbf{f}(y)$ is governed by the nondimensional Navier–Stokes equations

$$\partial_t \mathbf{v} + (\mathbf{v}\cdot\nabla)\mathbf{v} = -\nabla p + \frac{1}{\mathrm{Re}}\nabla^2\mathbf{v} + \mathbf{f}(y), \tag{1}$$

along with the incompressibility constraint

$$\nabla\cdot\mathbf{v} = 0. \tag{2}$$

Here and throughout, a Cartesian coordinate system is adopted in which x, y and z are the dimensionless streamwise, wall-normal and spanwise directions, respectively. The velocity

vector $\mathbf{v}$ has dimensionless components (u, v, w), and p is the dimensionless fluid pressure. In (1) all lengths have been scaled by H, i.e. half the (dimensional) distance separating the plane parallel walls, and all velocities by a characteristic velocity U. In PCF, U is the dimensional speed of the upper wall, the flow being driven by in-plane but opposing motion of the no-slip boundaries; in this case the body force vanishes: $\mathbf{f}(y) = \mathbf{0}$. This configuration admits a structureless laminar solution, namely Couette flow, as depicted in figure 1 (left panel). As is well known, this solution is linearly stable even for asymptotically large values of the Reynolds number $\mathrm{Re} \equiv UH/\nu$ [22, 23], although stability is observed experimentally only for $\mathrm{Re} < \mathrm{Re}_u \approx 310$ [24–26]. Careful parameter studies have revealed, for larger Reynolds numbers, a variety of structured flow regimes [27]: in $\mathrm{Re}_u < \mathrm{Re} < \mathrm{Re}_g \approx 325$, perturbations to Couette flow evolve into evanescent turbulent spots before Couette flow is restored. The lifetime of the transient spots diverges as Re_g is approached [28], indicating the onset of sustained turbulence above Re_g, where most of the turbulent spots survive and organize themselves into turbulent bands oblique to the streamwise direction [29, 30]. As Re is increased further, turbulence progressively invades the domain until $R_t \approx 415$, where space-filling turbulence is observed.

We focus here on a close relative of PCF, namely Waleffe flow (WF), depicted in figure 1 (right panel). This flow is driven by an x-directed body force that varies sinusoidally in the wall-normal direction, *viz.*, $\mathbf{f}(y) = \frac{\sqrt{2}\pi^2}{4\mathrm{Re}} \sin\left(\frac{\pi y}{2}\right) \hat{\mathbf{x}}$, where $\hat{\mathbf{x}}$ is a unit vector in the x direction. Moreover, stress-free rather than no-slip conditions are imposed along stationary boundaries located at $y = \pm 1$. This flow was suggested by Waleffe [2] as an alternative to PCF that is more convenient for low-order modeling. Indeed, WF can be naturally expanded in Fourier modes in all three coordinate directions, and the laminar basic state $\mathbf{v}=(\sqrt{2}\sin(\pi y/2),0,0)$ is itself a low-order mode in this basis. Note that in WF the velocity scale U is the root-mean-square velocity of the corresponding dimensional laminar base flow. Although this base flow has an inflection point, it is nevertheless linearly stable for all Re [18]. This is a consequence of the blocking effect of the walls at $y = \pm 1$; in contrast, the related Kolmogorov flow [31] is defined with periodic boundary conditions in y, thereby eliminating the stabilizing effect of the walls and permitting linear instability on large scales [32–34]. However, WF does admit finite amplitude solutions supported by the self-sustaining process identified by Waleffe [2]. These ECS also cannot bifurcate from the base flow, but instead appear through saddle-node bifurcations as Re increases, much as in PCF.

A. Multiscale analysis

In this section we derive the basic equations used in this paper. The procedure is motivated by earlier work on flows with strong restraints [35], particularly Langmuir circulation [36]. In these flows the strong restraining force reduces the effective dimensionality of the system, leading to a simplified description.

We begin by decomposing the velocity $\mathbf{v}$ into a streamwise component u and the perpen-

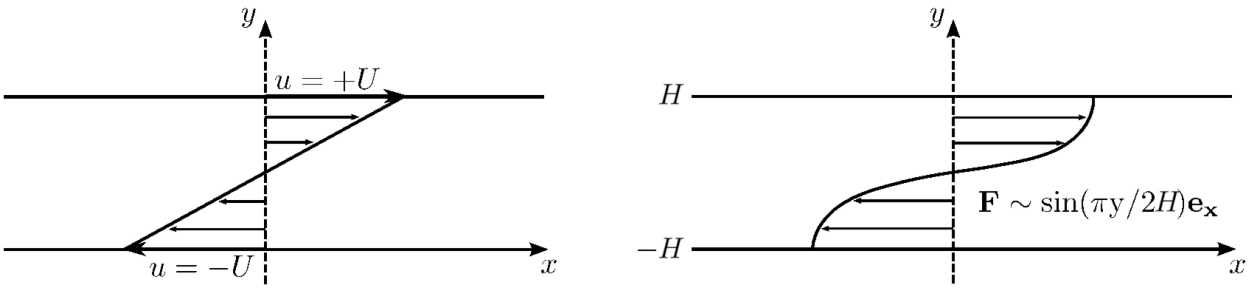

FIG. 1. Sketch of plane Couette and Waleffe flows. Plane Couette flow is driven by wall motion in the x direction, the top and bottom walls moving with opposite velocities $\pm U$. Plane Waleffe flow is driven by an x-directed body force. The forcing profile is a half-period of a sinusoid in y. Note that the laminar flow is stable despite the presence of an inflection point owing to the proximity of the (stress-free) walls.

dicular components $\mathbf{v}_\perp = (v, w)$, i.e., $\mathbf{v} \equiv (u, \mathbf{v}_\perp)$. Thus

$$\partial_t u + u\partial_x u + (\mathbf{v}_\perp \cdot \nabla_\perp)\, u = -\partial_x p + \frac{1}{\mathrm{Re}}\left(\partial_x^2 + \nabla_\perp^2\right) u + \frac{\sqrt{2}\pi^2}{4\mathrm{Re}} \sin\left(\frac{\pi y}{2}\right), \tag{3}$$

$$\partial_t \mathbf{v}_\perp + u\partial_x \mathbf{v}_\perp + (\mathbf{v}_\perp \cdot \nabla_\perp)\, \mathbf{v}_\perp = -\nabla_\perp p + \frac{1}{\mathrm{Re}}\left(\partial_x^2 + \nabla_\perp^2\right) \mathbf{v}_\perp, \tag{4}$$

$$\partial_x u + \nabla_\perp \cdot \mathbf{v}_\perp = 0. \tag{5}$$

These equations are supplemented with the following boundary conditions along the walls at $y = \pm 1$:

$$\partial_y u = v = \partial_y w = 0. \tag{6}$$

In addition, all fields are taken to be periodic in the streamwise and spanwise directions, with periods L_x and L_z, respectively.

To allow for slow modulation in the streamwise direction, we explicitly introduce a slow streamwise coordinate $X \equiv \epsilon x$ and an associated slow time scale $T \equiv \epsilon t$, where the small parameter $\epsilon \equiv 1/\mathrm{Re}$. Thus, all field variables are interpreted as functions of (x, X, y, z, t, T). Replacing the original x and t derivatives by $\partial_x + \epsilon\partial_X$ and $\partial_t + \epsilon\partial_T$, respectively, Eqns. (3)–(5) become

$$\begin{aligned}[\partial_t + \epsilon\partial_T]\, u + [\partial_x + \epsilon\partial_X]\, u^2 + \nabla_\perp \cdot (\mathbf{v}_\perp u) = &-[\partial_x + \epsilon\partial_X] p + \epsilon \frac{\sqrt{2}\pi^2}{4} \sin\left(\frac{\pi y}{2}\right) \\ &+\epsilon\left[\partial_x^2 + 2\epsilon\partial_X\partial_x + \epsilon^2\partial_X^2 + \nabla_\perp^2\right] u,\end{aligned} \tag{7}$$

$$\begin{aligned}[\partial_t + \epsilon\partial_T]\, \mathbf{v}_\perp + [\partial_x + \epsilon\partial_X]\, (u\mathbf{v}_\perp) + \nabla_\perp \cdot (\mathbf{v}_\perp \mathbf{v}_\perp) = &-\nabla_\perp p \\ &+\epsilon\left[\partial_x^2 + 2\epsilon\partial_X\partial_x + \epsilon^2\partial_X^2 + \nabla_\perp^2\right] \mathbf{v}_\perp,\end{aligned} \tag{8}$$

$$[\partial_x + \epsilon\partial_X]\, u + \nabla_\perp \cdot \mathbf{v}_\perp = 0. \tag{9}$$

Next, we decompose all variables into a fast (x,t) average plus a fluctuation with zero mean. For example, for the x velocity component, we write

$$u(x,X,y,z,t,T) = \bar{u}(X,y,z,T) + u'(x,X,y,z,t,T),$$

where the overbar denotes the fast (x,t) average. The motivation for averaging only in x rather than over the entire horizontal (x,z) plane is that nontrivial spanwise structure of the streamwise-averaged streamwise velocity, associated with the streamwise streaks, plays a crucial role in the process that sustains the streamwise rolls. With this decomposition, the mean equations can be expressed as

$$\epsilon\partial_T\bar{u} + \epsilon\partial_X\left[\bar{u}\bar{u} + \overline{u'u'}\right] + \nabla_\perp\cdot\left[\bar{\mathbf{v}}_\perp\bar{u} + \overline{\mathbf{v}'_\perp u'}\right] = -\epsilon\partial_X\bar{p} + \epsilon\nabla_\perp^2\bar{u} + \epsilon^3\partial_X^2\bar{u} + \epsilon\frac{\sqrt{2}\pi^2}{4}\sin\left(\frac{\pi y}{2}\right), \tag{10}$$

$$\epsilon\partial_T\bar{\mathbf{v}}_\perp + \epsilon\partial_X\left[\bar{u}\bar{\mathbf{v}}_\perp + \overline{u'\mathbf{v}'_\perp}\right] + \nabla_\perp\cdot\left[\bar{\mathbf{v}}_\perp\bar{\mathbf{v}}_\perp + \overline{\mathbf{v}'_\perp\mathbf{v}'_\perp}\right] = -\nabla_\perp\bar{p} + \epsilon\nabla_\perp^2\bar{\mathbf{v}}_\perp + \epsilon^3\partial_X^2\bar{\mathbf{v}}_\perp, \tag{11}$$

$$\epsilon\partial_X\bar{u} + \nabla_\perp\cdot\bar{\mathbf{v}}_\perp = 0. \tag{12}$$

We proceed by positing an appropriate expansion for the various fields. To this end, we are motivated in part by the scaling behavior identified in [16] and recalled in Sec. I for lower-branch ECS although we emphasize that the resulting reduced system is not limited to lower-branch states. For large Re the rolls comprising the streamwise-averaged flow in the perpendicular plane are weak, $O(1/\mathrm{Re})$, relative to the deviation of the streamwise-averaged streamwise flow from the base laminar profile (i.e., the streaks). A *closed*, self-consistent reduced model may be obtained by further positing that the (streamwise-varying) fluctuations are similarly weak relative to the mean streamwise flow, an assumption that is consistent with the scalings reported in table I. Thus, we expand the velocity components and pressure as follows:

$$u \sim (\bar{u}_0 + u'_0) + \epsilon(\bar{u}_1 + u'_1) + \ldots, \tag{13}$$

$$\mathbf{v}_\perp \sim \epsilon(\bar{\mathbf{v}}_{1\perp} + \mathbf{v}'_{1\perp}) + \epsilon^2(\bar{\mathbf{v}}_{2\perp} + \mathbf{v}'_{2\perp}) + \ldots, \tag{14}$$

$$p \sim (\bar{p}_0 + p'_0) + \epsilon(\bar{p}_1 + p'_1) + \epsilon^2(\bar{p}_2 + p'_2) + \ldots \tag{15}$$

At $O(1)$, Eqs. (7)–(9) imply

$$\partial_t u'_0 + (\bar{u}_0 + u'_0)\partial_x u'_0 = -\partial_x p'_0, \tag{16}$$

$$0 = -\nabla_\perp(\bar{p}_0 + p'_0), \tag{17}$$

$$\partial_x u'_0 = 0. \tag{18}$$

From this equation set we conclude that $u'_0 \equiv 0$ and $p'_0 \equiv 0$. Note that $\bar{p}_0$, if nonzero, can only depend on X and T; this term is set to zero for PCF and WF, but may be retained for flows driven by externally-imposed mean pressure gradients (such as plane Poiseuille flow).

Using these leading-order results, Eq. (7) yields at $O(\epsilon)$

$$\partial_t u'_1 + \partial_T\bar{u}_0 + \bar{u}_0\partial_x u'_1 + \bar{u}_0\partial_X\bar{u}_0 + \left[(\bar{\mathbf{v}}_{1\perp} + \mathbf{v}'_{1\perp})\cdot\nabla_\perp\right]\bar{u}_0 = -\partial_x p'_1 - \partial_X\bar{p}_0 + \nabla_\perp^2\bar{u}_0 + \frac{\sqrt{2}\pi^2}{4}\sin\left(\frac{\pi y}{2}\right). \tag{19}$$

Averaging this equation over the fast x and t variables, and using the fact that $\bar{p}_0 \equiv 0$ for both PCF and WF, we obtain

$$\partial_T \bar{u}_0 + \bar{u}_0 \partial_X \bar{u}_0 + (\bar{\mathbf{v}}_{1\perp} \cdot \nabla_\perp)\, \bar{u}_0 = -\partial_X \bar{p}_0 + \nabla_\perp^2 \bar{u}_0 + \frac{\sqrt{2}\pi^2}{4} \sin\left(\frac{\pi y}{2}\right). \tag{20}$$

Subtracting Eq. (20) from Eq. (19) yields an equation for the streamwise fluctuating velocity u_1':

$$\partial_t u_1' + \bar{u}_0 \partial_x u_1' + (\mathbf{v}_{1\perp}' \cdot \nabla_\perp)\, \bar{u}_0 = -\partial_x p_1'. \tag{21}$$

At $O(\epsilon)$, the perpendicular momentum equation (8) takes the form

$$\partial_t \mathbf{v}_{1\perp}' + \bar{u}_0 \partial_x \mathbf{v}_{1\perp}' = -\nabla_\perp (\bar{p}_1 + p_1'), \tag{22}$$

from which we conclude that

$$\nabla_\perp \bar{p}_1 = 0 \tag{23}$$

and

$$\partial_t \mathbf{v}_{1\perp}' + \bar{u}_0 \partial_x \mathbf{v}_{1\perp}' = -\nabla_\perp p_1'. \tag{24}$$

Finally, the $O(\epsilon)$ continuity equation requires

$$\partial_X \bar{u}_0 \; + \; \nabla_\perp \cdot \bar{\mathbf{v}}_{1\perp} = 0 \tag{25}$$

and

$$\partial_x u_1' \; + \; \nabla_\perp \cdot \mathbf{v}_{1\perp}' = 0. \tag{26}$$

To obtain a closed reduced system, we average the $O(\epsilon^2)$ perpendicular momentum equation,

$$\begin{aligned} \partial_t \mathbf{v}_{2\perp}' + \partial_T(\bar{\mathbf{v}}_{1\perp} + \mathbf{v}_{1\perp}') + \bar{u}_0 \partial_x \mathbf{v}_{2\perp}' + (\bar{u}_1 + u_1')\partial_x \mathbf{v}_{1\perp}' + \bar{u}_0 \partial_X (\bar{\mathbf{v}}_{1\perp} + \mathbf{v}_{1\perp}') \\ + \left[(\bar{\mathbf{v}}_{1\perp} + \mathbf{v}_{1\perp}') \cdot \nabla_\perp\right] (\bar{\mathbf{v}}_{1\perp} + \mathbf{v}_{1\perp}') \;=\; -\nabla_\perp (\bar{p}_2 + p_2') \\ + \left(\partial_x^2 + \nabla_\perp^2\right) (\bar{\mathbf{v}}_{1\perp} + \mathbf{v}_{1\perp}'), \end{aligned} \tag{27}$$

and obtain, on using Eq. (26), the following equation for the evolution of $\bar{\mathbf{v}}_{1\perp}$:

$$\partial_T \bar{\mathbf{v}}_{1\perp} + \partial_X \left[\bar{u}_0 \bar{\mathbf{v}}_{1\perp}\right] + \nabla_\perp \cdot \left[\bar{\mathbf{v}}_{1\perp} \bar{\mathbf{v}}_{1\perp} + \overline{\mathbf{v}_{1\perp}' \mathbf{v}_{1\perp}'}\right] = -\nabla_\perp \bar{p}_2 + \nabla_\perp^2 \bar{\mathbf{v}}_{1\perp}. \tag{28}$$

The fluctuation equations (21) and (24) are linear and non-dissipative and hence the steady version of these equations exhibits a critical-layer singularity. For this reason these equations require an appropriate regularization before the above equation set can be used to compute ECS. This procedure is discussed next.

B. Structure and regularization of the reduced model

For ease of reference, we collect here the key results of the analysis. Specifically, the multiscale reduced model consists of Eq. (20), with $\bar{p}_0 \equiv 0$, Eqs. (28) and (25),

$$\partial_T \bar{u}_0 + \bar{u}_0 \partial_X \bar{u}_0 + (\bar{\mathbf{v}}_{1\perp} \cdot \nabla_\perp)\, \bar{u}_0 = \nabla_\perp^2 \bar{u}_0 + \frac{\sqrt{2}\pi^2}{4} \sin\left(\frac{\pi y}{2}\right), \tag{29}$$

$$\partial_T \bar{\mathbf{v}}_{1\perp} + \partial_X \left[\bar{u}_0 \bar{\mathbf{v}}_{1\perp}\right] + \nabla_\perp \cdot \left[\bar{\mathbf{v}}_{1\perp}\bar{\mathbf{v}}_{1\perp} + \overline{\mathbf{v}'_{1\perp}\mathbf{v}'_{1\perp}}\right] = -\nabla_\perp \bar{p}_2 + \nabla_\perp^2 \bar{\mathbf{v}}_{1\perp}, \tag{30}$$

$$\partial_X \bar{u}_0 \, + \, \nabla_\perp \cdot \bar{\mathbf{v}}_{1\perp} = 0, \tag{31}$$

which govern the mean (i.e., fast x and t averaged) dynamics, and Eqs. (21), (24) and (26), appropriately regularized,

$$\partial_t u'_1 + \bar{u}_0 \partial_x u'_1 + (\mathbf{v}'_{1\perp} \cdot \nabla_\perp)\, \bar{u}_0 = -\partial_x p'_1 \, + \, \epsilon \nabla_\perp^2 u'_1, \tag{32}$$

$$\partial_t \mathbf{v}'_{1\perp} + \bar{u}_0 \partial_x \mathbf{v}'_{1\perp} = -\nabla_\perp p'_1 \, + \, \epsilon \nabla_\perp^2 \mathbf{v}'_{1\perp}, \tag{33}$$

$$\partial_x u'_1 \, + \, \nabla_\perp \cdot \mathbf{v}'_{1\perp} = 0, \tag{34}$$

for the fluctuating fields. These equations are to be solved subject to the mean and fluctuating boundary conditions obtained by applying the mean/fluctuation decomposition to the conditions (6), *viz.*,

$$\partial_y \bar{u}_0 = \partial_y u'_1 = \bar{v}_1 = \partial_y \bar{w}_1 = v'_1 = \partial_y w'_1 = 0 \tag{35}$$

on $y = \pm 1$.

Physically, the averaged equations constrain the slow temporal and streamwise evolution of the streaks ($\bar{u}_0$) and rolls ($\bar{\mathbf{v}}_{1\perp}$). The presence of an effective Reynolds number equal to unity (the prefactor in front of the Laplacian in Eqs. (29) and (30) equals one), together with the absence of fast streamwise and temporal variation, suggests that these equations should be more computationally tractable than the full Navier–Stokes equations at large Re. Indeed, if the slow streamwise (X) variation is suppressed, the averaged equations are spatially 2D and may be expected to exhibit quasi-laminar behavior. Thus, deviations from the base laminar flow, if nonzero, are driven *solely* by the fluctuation-induced Reynolds stress divergence in Eq. (30); this correlation involves only the perpendicular fluctuating velocity field, all other Reynolds stress components being smaller than the retained mean terms.

Presuming fluctuation gradients remain $O(1)$, the fluctuating fields themselves evolve in accord with the equations governing the *inviscid stability* of streamwise streaks (under the consistent approximation that the $O(1/\mathrm{Re})$ rolls may be neglected). In particular, spanwise inflections in the profile of $\bar{u}_0(X, y, z, T)$ may be expected to give rise to an x-varying 3D instability whose primary effect will be to re-energize the streamwise rolls through the Reynolds stress term, in accord with the self-sustaining process of Waleffe [2]. As explicitly demonstrated in [16], the fluctuation (or wave) fields, which are necessarily steady (neutral) for equilibrium ECS, exhibit a critical layer structure along the isosurface $\bar{u}_0(y, z)$=0. In the neighborhood of the critical layer, the fluctuation gradients are large, resulting in a distinct leading-order dominant balance involving diffusion. In Eqs. (32) and (33) this balance is captured, as in [17], by retaining the formally small diffusion terms $\epsilon \nabla_\perp^2 u'_1$ and $\epsilon \nabla_\perp^2 \mathbf{v}'_{1\perp}$,

respectively, where $\epsilon \equiv 1/\mathrm{Re}$. From the point of view of asymptotics the retention of these terms may be justified by appeal to the method of *composite asymptotic approximations* or to the related method of *composite asymptotic equations* [37] but in our reduced model these terms are retained because they capture correctly the broadening of the critical layer in the transition region that is of interest here. A similar regularization was employed in recent work on high Reynolds number Couette flow by Blackburn *et al.* [14] in order to avoid the intricacies associated with carrying out a systematic matched asymptotic analysis valid in the limit $\mathrm{Re} \to \infty$ [13].

It is important to compare our approach with that of Hall & Sherwin [13] and Blackburn *et al.* [14] in more detail. The analysis of Hall & Sherwin [13] demonstrates that in the limit $\mathrm{Re} \to \infty$ the amplitude of the fluctuating fields in the Nagata–Busse/Clever–Waleffe lower-branch PCF equilibrium solution scales as $\mathrm{Re}^{-7/6}$ – not Re^{-1} – away from the critical layer. Within the critical layer, the fluctuation velocity components tangent to the critical layer are amplified, becoming $O(\mathrm{Re}^{-5/6})$ – again rather than $O(\mathrm{Re}^{-1})$ as prescribed here. Thus, in the limit $\mathrm{Re} \to \infty$, the fluctuation-induced forcing of the rolls is asymptotically confined to the critical layer, justifying the jump condition formulation derived in [13]. In contrast, our reduced equations are not optimised to capture the properties of ECS in the limit $\mathrm{Re} \to \infty$. Instead the equations have been developed for transition values of the Reynolds number where no singular critical layer is present and one can confirm that all of the terms required to capture the physics of this region are retained. Since our procedure leads ultimately to the retention of the same terms as that of Hall & Sherwin [13] and Blackburn *et al.* [14] it follows that our fluctuations will grow near the critical layer and decay away from it with increasing Re when Re is very large. This is not an issue since we apply our equations in the transition regime where ECS are known to be dynamically relevant [16]. In this regime the results of Wang *et al.* [16] indicate that the scale separation between the magnitude of the fluctuation/roll fields and the streak field, on which the reduced model is founded, is already evident. Moreover, at these moderate values of Re (e.g., $\mathrm{Re} = O(10^3)$), the quantity $\mathrm{Re}^{-1/3}$ is not particularly small, and the distinction between the fluctuation amplitude within and outside the critical layer becomes blurred. Of course, there may also be other, perhaps non-equilibrium (e.g., a periodic-orbit) ECS that do *not* exhibit critical layer structure at all but that can nevertheless be captured by our self-consistent reduced model.

It is significant that the fluctuation equations (32)–(34) do not mix x modes, a fact we exploit in our computations of ECS for WF using the reduced system. Specifically and in accord with the scalings given in table I, we retain only the fundamental streamwise Fourier mode for each fluctuation field, and write

$$u_1'(x,y,z,t) = \hat{u}_1(y,z,t)e^{i\alpha x} + c.c., \tag{36}$$

where $\alpha \equiv 2\pi/L_x$ is the dimensionless fundamental streamwise wave number and *c.c.* denotes the complex conjugate; similar expressions are written for v_1', w_1' and p_1'. In the following, we drop the hat over fluctuating variables for brevity of notation. In very long domains a nearly continuous band of modes with similar streamwise wave numbers will be neutral or very weakly damped, leading to a description of the flow in terms of an evolving linear superposition of these modes exhibiting a slowly-varying envelope. This evolution will in

turn drive slow streamwise modulations of the mean fields through the Reynolds stress divergence term in Eq. (30). A mechanism of this type may provide an explanation for the streamwise localization of ECS observed in a variety of plane parallel shear flows [12], further attesting to the value of the reduced structure identified here.

In the first instance, however, slow streamwise variations can be suppressed. The resulting averaged equations (29)–(31) can then be further simplified by introducing a streamwise-invariant streamfunction ϕ_1: $\bar{v}_1 = -\partial_z\phi_1$, $\bar{w}_1 = \partial_y\phi_1$, yielding the streamwise-invariant vorticity $\omega_1 = \nabla_\perp^2\phi_1$. Consequently, the averaged system can be expressed as

$$\partial_T u_0 + J(\phi_1, u_0) = \nabla_\perp^2 u_0 + \tfrac{\sqrt{2}\pi^2}{4}\sin(\pi y/2), \tag{37}$$

$$\partial_T\omega_1 + J(\phi_1,\omega_1) + 2(\partial_{yy}^2 - \partial_{zz}^2)\left(\mathcal{R}(v_1 w_1^*)\right) + 2\partial_y\partial_z(w_1 w_1^* - v_1 v_1^*) = \nabla_\perp^2\omega_1, \tag{38}$$

where $J(\phi_1, f) = \partial_y\phi_1\partial_z f - \partial_z\phi_1\partial_y f$ and $\mathcal{R}$ denotes the real part. In writing these equations, we have dropped the overbar on the mean streamwise velocity component u_0, again for notational brevity. The fluctuation equations can also be simplified, in particular by taking the divergence of Eqs. (32) and (33) and using Eq. (34) to obtain a Helmholtz equation for the pressure p_1. The resulting fluctuation equations can be written in the form

$$(\alpha^2 - \nabla_\perp^2)p_1 = 2i\alpha(v_1\partial_y u_0 + w_1\partial_z u_0), \tag{39}$$

$$\partial_t\mathbf{v}_{1\perp} + i\alpha u_0\mathbf{v}_{1\perp} = -\nabla_\perp p_1 + \epsilon\nabla_\perp^2\mathbf{v}_{1\perp}. \tag{40}$$

The boundary conditions at $y = \pm 1$ are

$$\partial_y u_0 = \omega_1 = \phi_1 = v_1 = \partial_y w_1 = 0, \tag{41}$$

together with periodic boundary conditions in z. Observe that u_1 does not appear in these equations although it can be recovered from Eq. (34).

Equations (37)–(40) capture the self-sustaining process explicitly: the rolls ω_1 (ϕ_1) deform the structure of the streamwise velocity u_0 to generate streaks as described by Eq. (37). These streaks lead to the formation of a fluctuating structure $\mathbf{v}_{1\perp}$ through the advection term in Eq. (40). Lastly, these fluctuations feed the rolls through the Reynolds stresses in Eq. (38). The reduced model (37)–(40) thus isolates the self-sustaining process described by Waleffe [2].

III. NUMERICAL STRATEGY

A common approach for computing edge solutions is to apply a so-called edge-tracking algorithm, which only requires use of a time-stepper for the equations [38, 39]. In the present case, however, implementation of this technique is complicated by the occurrence of two time scales t and $T = \epsilon t = t/\mathrm{Re}$ in our reduced equations: the mean variables u_0, ω_1 evolve on the long time scale T, while the fluctuating variables $\mathbf{v}_{1\perp}$ and p_1 vary on the fast time scale t. In the small ϵ limit, the slow mean variables are quasi-steady during the evolution of the fast fluctuating variables. Thus, the fluctuation equations (39)–(40) are effectively quasi-linear, and the mean variables only respond to the evolution of the fluctuations on a longer time scale. Systems of this type are best solved by treating the fluctuation system as an

eigenvalue problem [17], thereby avoiding edge tracking altogether; a similar strategy was followed by Hall & Sherwin [13] and Blackburn *et al.* [14].

We now describe the details of our algorithm. We consider a two-dimensional domain $\mathcal{D}$ initially of size $L_y \times L_z = 2 \times \pi$, where $L_y = 2$ is the (dimensionless) distance between the walls and $L_z = \pi$ is the (dimensionless) imposed period in the spanwise direction, and set the streamwise wave number $\alpha = 0.5$. For PCF this domain yields the least unstable lower branch solution [40]. The two-dimensional domain is meshed using equidistributed points and the solutions expressed in a Fourier basis. The equations are treated in spectral space using the Fast Fourier Transform in the periodic direction z and either the Fast Cosine Transform-I or Fast Sine Transform-I in the wall-bounded direction y, depending on the boundary conditions: u_0 and w_1 are expanded in a cosine basis while ω_0 and v_1 are expanded in a sine basis [41]. All spatial derivatives are computed pseudospectrally in physical space. The usual 2/3 dealiasing is applied for quadratic nonlinearities to avoid mode contamination by spectral convolution.

By analogy with PCF we seek solutions that are shift-reflect-symmetric, i.e., solutions that are invariant under the operation $[u, v, w](x, y, z) = [u, v, -w](x+L_x/2, y, -z)$, where L_x is the imposed period in the streamwise direction – in our case $L_x = 4\pi$. Within the reduced model framework, this operation becomes $[u_0, \omega_1, v_1, w_1](y, z) = [u_0, -\omega_1, -v_1, w_1](y, -z)$. In addition, the solutions can be translated in x: $[u, v, w](x, y, z) \to [u, v, w](x + \ell, y, z)$, where ℓ is an arbitrary real quantity. Within our approach this symmetry corresponds to $[u_0, \omega_1, v_1, w_1](y, z) \to [u_0, \omega_1, \mathcal{R}(v_1)\cos(\ell') - \mathcal{I}(v_1)\sin(\ell') + i(\mathcal{R}(v_1)\sin(\ell') + \mathcal{I}(v_1)\cos(\ell'))$, $\mathcal{R}(w_1)\cos(\ell') - \mathcal{I}(w_1)\sin(\ell') + i(\mathcal{R}(w_1)\sin(\ell') + \mathcal{I}(w_1)\cos(\ell'))](y, z)$, where $\mathcal{R}(\cdot)$ (resp. $\mathcal{I}(\cdot)$) denotes the real (resp. imaginary) part and $\ell' \equiv \alpha\ell$.

The numerical algorithm for solving the above problem consists of two parts, an iterative strategy to obtain a good initial condition (described in Sec. III A) and a Newton method to converge the initial condition to an exact ECS solution of the reduced model (37)–(40) (described in Sec. III B). The latter step requires a novel preconditioner also described in Sec. III B. This two-step process forms the basis for our numerical continuation of the resulting ECS in $\mathrm{Re} \equiv \epsilon^{-1}$.

A. The initial iterate

We start by decoupling the mean variables u_0 and ω_1 that evolve slowly from the fluctuations v_1 and w_1 that evolve more rapidly. We thus consider in succession the slow equations (37) and (38) in which the Reynolds stresses are fixed, and the fast equations (39) and (40) in which the quantity u_0 is maintained constant. Within this framework, the fluctuation equations are linear and autonomous. We take advantage of this structure by treating the fluctuation system as an eigenvalue problem, i.e., we seek solutions with exponential dependence in time: $\mathbf{v_1}_\perp(y, z, t) \equiv \hat{\mathbf{v}}_{\mathbf{1}\perp}(y, z)e^{\lambda t}$ and $p_1(y, z, t) \equiv \hat{p}_1(y, z)e^{\lambda t}$, where λ is the growth rate of the fluctuations. This approach is critical as it provides more information on the fast dynamics than is available with time-steppers, which only determine the dominant modes. The basic idea is straightforward: if one of the fluctuating modes is marginal, it corresponds to a stationary solution of the fluctuation equations and if the associated mean variables are

also stationary, then the combined mean/fluctuation fields comprise a stationary solution of the reduced system (37)–(40).

The separate treatment of the mean and fluctuation problems implies that the scalar amplitude of the fluctuations in Eqs. (39) and (40) is not fixed by the eigenvalue solve, but must be self-consistently determined as part of the iterative procedure. We refer to this *a priori* unknown scalar as A and define it mathematically in Sec. IV. Finding a solution of the problem (37)–(40) is then equivalent to finding the correct fluctuation amplitude A for which, given stationary mean variables u_0 and ω_1, there exists a fluctuating mode with vanishing growth rate. To obtain a good first approximation to an ECS for subsequent refinement and continuation via Newton iteration, we use the following multi-step iterative algorithm:

1. Arbitrarily choose the fluctuation amplitude A
2. If the growth rate λ of the fastest non-oscillatory growing (or slowest decaying) mode is nonzero:
   - 2.1. Compute the fastest non-oscillatory growing (or slowest decaying) fluctuating mode and its growth rate λ from equations (39) and (40)
   - 2.2. Time-advance u_0 and ω_1 to steady state using equations (37) and (38)
   - 2.3. Repeat steps 2.1 and 2.2 until a converged growth rate $\lambda(A)$ is obtained
3. Adjust A to drive $\lambda(A)$ to zero by repeating steps 2.1–2.3.

Although developed for canonical wall-bounded shear flows [17] we mention that a similar procedure has been employed with considerable success in a recent study of the saturation of the von Kármán vortex shedding instability of the flow past a cylinder [42].

To use the above algorithm, an initial condition for u_0 alone is required. Solutions of the eigenvalue problem in step 2.1 are obtained using the exponential power method and the package ARPACK [43]. Note that this computation is equivalent to finding the stability of u_0 with respect to streamwise fluctuating perturbations of wave number α. As we are interested in the least unstable, and hence the most dynamically influential, solutions, we focus on the fastest growing or slowest decaying mode. Other equilibria or periodic orbits may be found by looking at subsequent eigenvalues but this is outside the scope of the present paper. The time integration of Eqs. (37) and (38) in step 2.2 is carried out using a semi-implicit third-order Runge–Kutta scheme [44]. This step is very fast compared to the eigenvalue computation. To simplify the entire computation, we impose the shift-reflect symmetry during the eigenvalue search and the time integration of the mean equations.

B. Preconditioned Newton method

Following the computation of good approximates using the iterative algorithm just described, the final step is to converge these solutions to the desired accuracy. Typically, this is done using a Newton method for which an inner iteration is required to invert a certain

Jacobian matrix that we define below. The Jacobian resulting from the reduced system (37)–(40) is poorly conditioned and complicates the use of a Newton method. A suitable preconditioner is therefore required and we designed one based on that originally proposed by Tuckerman [45, 46]. Here, we describe its implementation on the generic system

$$\gamma_t \partial_t U = N(U) + \gamma_D L U, \tag{42}$$

where U is the dependent variable, N is a nonlinear operator, L is a linear (Laplace) operator, with γ_t, γ_D real constants. We look for stationary solutions and so aim to solve

$$0 = N(U) + \gamma_D L U. \tag{43}$$

The preconditioner introduced by Tuckerman is constructed from an implicit Euler scheme with time-step $\triangle t$ applied to Eq. (42):

$$U(t+\triangle t) = \left(I - \frac{\triangle t\, \gamma_D}{\gamma_t} L\right)^{-1} \left(U(t) + \frac{\triangle t}{\gamma_t} N(U(t))\right), \tag{44}$$

where $U(t)$ stands for the value of U at time t and I represents the identity operator. We note that by substracting $U(t)$ from expression (44), we obtain

$$U(t+\triangle t) - U(t) = \frac{\triangle t}{\gamma_t} \left(I - \frac{\triangle t\, \gamma_D}{\gamma_t} L\right)^{-1} \left(N(U(t)) + \gamma_D L U(t)\right), \tag{45}$$

where the right hand side of Eq. (43) is recovered and preconditioned by $P = I - \triangle t\, \gamma_D/\gamma_t\, L$.

A Newton method can be obtained by writing for iterate $U^{[k]}$ at iteration k

$$N(U^{[k]}) + \gamma_D L U^{[k]} = J(U^{[k]})\, \delta U, \tag{46}$$

solving for δU and correcting $U^{[k+1]} = U^{[k]} - \delta U$. In writing Eq. (46), we have introduced $J(U^{[k]}) = \delta N(U^{[k]}) + \gamma_D L$, the Jacobian of the right hand side operator in Eq. (42) with $\delta N(U^{[k]}) \equiv \delta N/\delta U(U^{[k]})$. On multiplying both sides of Eq. (46) by $\triangle t/\gamma_t\, P^{-1}$, one obtains

$$\frac{\triangle t}{\gamma_t} P^{-1} \left(N(U^{[k]}) + \gamma_D L U^{[k]}\right) = \frac{\triangle t}{\gamma_t} P^{-1} J(U^{[k]})\, \delta U. \tag{47}$$

The left hand side of Eq. (47) can be obtained directly using Eq. (45) by computing one implicit Euler time-step of the full equation (42) and substracting the initial condition. Moreover, applying the same method to Eq. (42) linearized around $U^{[k]}$ we obtain a linearized version of Eq. (45) that can then be used to calculate the right hand side of Eq. (47). In the small $\triangle t$ limit, $P \approx I$ and the equation is not preconditioned while for sufficiently large $\triangle t$, we get the so-called Stokes preconditioner $P \approx \triangle t(\gamma_D/\gamma_t)L$. This preconditioning method is easy to implement as it only requires a first order implicit Euler time-integration scheme and its use is natural within matrix-free methods, where the Jacobian is not explicitly constructed. The Stokes preconditioner has been widely used in problems that are dominated by diffusion like coupled convection [47–49]. In contrast, most shear flow studies are carried

out at large Reynolds numbers and involve weakly diffusive flows. The required computations are then often performed without preconditioning [50, 51].

In the present case, none of these approaches was efficient and we extended the previous preconditioning method to develop a mixed preconditioner. We note that the Jacobian is influenced by two terms: the linearized nonlinear term and the diffusive operator: $J(U) = \delta N(U) + \gamma_D L$. In the case of weakly diffusive flows, $\gamma_D \ll 1$ and the spectrum of the Jacobian is dominated by modes resulting from $\delta N(U)$. This is what happens in large Reynolds number studies. On the other hand, in the aforementioned convection problems $\gamma_D = O(1)$. These problems are poorly conditioned due to the prominence of eigenvalues generated by the diffusion operator. This difficulty is natural and can be understood by the following heuristic argument: on a given Fourier grid, the condition number of a periodic Laplace operator scales in proportion to k^2, where k is the largest wave number allowed. Thus accuracy is reached at the expense of poorer conditioning. This difficulty is typically handled by the use of Stokes preconditioning. In our reduced model, the mean equations (37) and (38) are diffusion-dominated: $\gamma_t = \epsilon^{-1}$ and $\gamma_D = 1$. According to the above considerations, these equations require Stokes-type preconditioning and we have found that $\triangle t = \epsilon^{-1} = \mathrm{Re}$ (hence $\triangle t \gamma_D / \gamma_t = 1$ such that $P = I - L$) provides good results. The fluctuation equation (40), with Eq. (39) solved as a preliminary step, is weakly diffusive with $\gamma_t = 1$ and $\gamma_D = \epsilon$ but was not efficiently solved without preconditioning. To improve the efficiency, we observed that the contribution of the nonlinear and the diffusive terms to the Jacobian depends strongly on the gradients within the critical layer. For the lower branch solution, the width of this layer scales like $(\alpha \mathrm{Re})^{-1/3}$, yielding a diffusion operator $(1/\mathrm{Re})\nabla_\perp^2 = O(\alpha^{2/3}\mathrm{Re}^{-1/3}) = O(\alpha^{2/3}\epsilon^{1/3})$. We incorporate this scaling by setting $\triangle t = \xi^2 \alpha^{2/3} \epsilon^{-2/3}$, such that $P = I - \xi^2 \alpha^{2/3} \epsilon^{1/3} L$, where $\xi = O(1)$ is a tuning constant. Several values of ξ were tested and we adopted $\xi = 0.5$ for the computations that follow, unless stated otherwise.

To compute the desired ECS using a Newton search we embed the biconjugate-gradient-squared routine from NSPCG [52] within the Newton algorithm and impose a shift-reflect symmetry on the solutions of Eqs. (37)–(40). Extra care is necessary to eliminate errors arising from the x-invariance of the solutions. Within our Fourier decomposition, translations correspond to the eigenvector $[u_0, \omega_1, v_1, w_1](y, z) = [0, 0, iv_1, iw_1](y, z)$. The evaluation of the left side of the system corresponding to Eq. (47) is carried out without any constraint while the right side is projected onto the space orthogonal to the above eigenvector, thereby removing the singularity of the Jacobian arising from translation invariance of the solution in x. The above procedure is implemented at each step of the Newton search and forms part of the continuation algorithm used to continue the converged solutions in parameter space.

The above procedure generates numerically exact stationary solutions of the reduced model (37)–(40) for fixed values of the Reynolds number Re, the streamwise wave number α and the cross-stream domain size. These converged ECS are characterized by a self-consistently determined amplitude A of the fluctuations that is required to distort the mean velocity profile in just such a way that the fluctuations neither grow nor decay. Thus A also provides a convenient measure of the nonlinear distortion of the streamwise velocity, and we can use it to track the evolution of the self-consistent ECS with the Reynolds number Re, the streamwise wave number α or the cross-stream domain size, just like other measures of

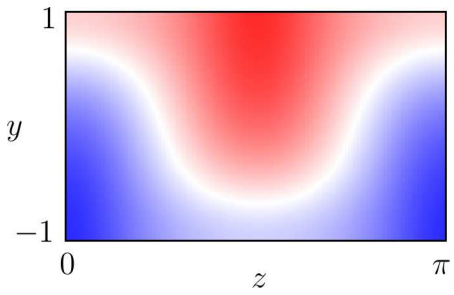

FIG. 2. (Color online) Initial condition for the iterative algorithm obtained by advecting/diffusing u_0 given a steady roll structure with $\omega_1(y,z) = 20\sin(\pi/2y)\sin(2z)$. The upper red (resp. lower blue) region has $u_0 > 0$ (resp. $u_0 < 0$.

the solution such as kinetic energy or maximum vorticity.

IV. EXACT COHERENT STATES

In this section, we present the ECS we have computed using the reduced model (37)–(40) with stress-free boundary conditions (41) at $y = \pm 1$ and periodic boundary conditions in z.

A. Initial search

We set $\mathrm{Re} = 400$ (or equivalently $\epsilon = 1/400$) and employ the iterative strategy introduced in Sec. III on a 32×32 mesh. The accuracy of the results presented here is confirmed by computations on a 64×64 grid. We recall that the use of the iterative algorithm introduced in Sec. III A only requires an initial condition on u_0. We generate such an initial condition by advecting the structureless Waleffe flow by a steady sinusoidal roll, $\omega_1(y,z) = 20\sin(\pi/2)\sin(2z)$ (or equivalently $\phi_1(y,z) = -5(\pi^2/16+1)^{-1}\sin(\pi/2y)\sin(2z)$), integrating Eq. (37) with a fixed ϕ_1 until a steady state is reached. The roll structure and amplitude have been chosen such that the resulting initial condition on u_0 resembles the ECS in PCF [13, 16, 40]. The resulting initial profile for the iterative algorithm is shown in figure 2.

We define the amplitude of the fluctuations numerically as the maximum value of any component of the in-plane fluctuating velocities on the meshgrid:

$$A = \max\left(|v_1(y_i,z_j)|;|w_1(y_i,z_j)|\right) \qquad \text{for } i = 1,M,\ j = 1,N, \tag{48}$$

where y_i (resp. z_j) represents the i-th (resp. j-th) meshpoint in y (resp. z), M and N are the number of points in y and z, and $|f| = \sqrt{f_r^2 + f_i^2}$ where the subscript r (resp. i) denotes the real (resp. imaginary) part. We employed the iterative algorithm for different values of A and observed two distinct regimes with different behavior of the leading real eigenvalue. In the first regime, observed for $A \le A_H \approx 6.81$, the leading real eigenvalue converges to $\lambda = \lambda_c(A)$. This regime is illustrated in figure 3(a). For $A = 0$ the solution converges to the Waleffe flow but as A increases the converged flow departs from WF. For $A > A_H$,

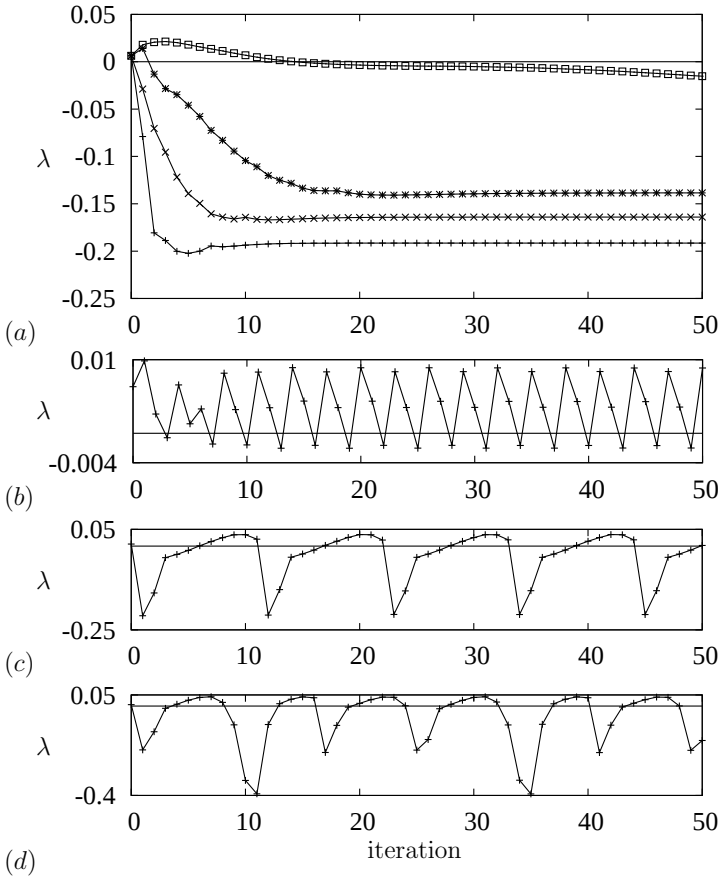

FIG. 3. (a) Steady regime of the iterative algorithm ($A \leq A_H \approx 6.81$). The curves represent the value of the largest real eigenvalue λ plotted against the iteration number. Only the first 50 iterations are shown and the curves correspond to $A = 5$, $A = 5.5$, $A = 6$ and $A = 6.5$ from bottom to top. The $A = 6.5$ eigenvalue converges at a later iteration (not shown). The oscillatory regime ($A > A_H$) is represented in the same way for $A = 6.9$ in (b), $A = 7.5$ in (c) and $A = 8$ in (d). In all cases, the algorithm is initialized using the initial condition shown in figure 2.

a second regime is present in which the algorithm does not converge but instead displays undamped oscillations (figures 3(b)–(d)). During the oscillations, the streaks u_0 alternately decay towards the trivial solution and then regrow into a more nonlinear structure that exaggerates the traits of the exact coherent state, a process that repeats in a periodic fashion. This process is straightforward for sufficiently small values of A but becomes increasingly complex as A is increased. For example, the oscillations in λ and the accompanying solution have a period of only 6 iterations for $A = 6.9$ (figure 3(b)) but 11 iterations per oscillation for $A = 7.5$ and 23 iterations per oscillation for $A = 8$ with λ showing increasingly complex behavior (figures 3(c,d)).

The difference between these two regimes can be traced to the way in which A, the scalar amplitude of the fluctuations, enters Eq. (38), where the Reynolds stress term has amplitude A^2. For a given fluctuation mode, increasing (decreasing) A leads to a greater (lesser) forcing of the rolls ω_1. The induced rolls deform the streaks u_0 generating a new eigenvalue problem

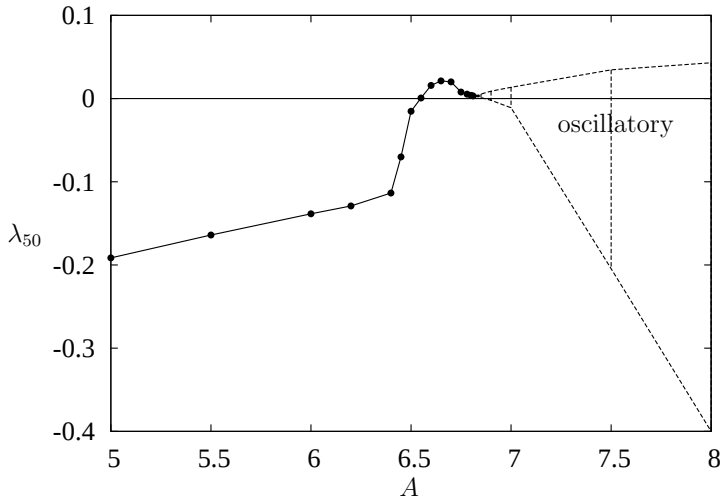

FIG. 4. The leading stationary eigenvalue λ_{50} after 50 iterations of the algorithm in the steady regime ($A \leq A_H \approx 6.81$) shown using a solid line with the dots indicating the value actually computed. Most of these eigenvalues decrease by less than 10^{-4} per iteration after 50 iterations. The eigenvalues for $6.4 \leq A \leq 6.6$ (corresponding to the region of steepest increase in the figure) are not fully converged after 50 iterations but do converge to slightly smaller values after a larger number of iterations. In fact convergence is not required as the aim is to generate a good initial condition for subsequent refinement by the preconditioned Newton method. The amplitude of the eigenvalue oscillations after 50 iterations in the oscillatory regime ($A > A_H$) is indicated by vertical dashed lines at the values of A actually used.

for the fluctuations. Hence, A is a forcing parameter that tunes one step in the self-sustaining process. If the forcing is too weak, the iterative algorithm relaxes to the trivial solution perturbed by a latent forcing induced by the non-vanishing fluctuations. If the forcing is too strong, the feedback from the mean variables (rolls ω_1, then streaks u_0) is also too strong, causing overshooting of a potential "steady" solution of the iterative algorithm. Since A is fixed during the iteration process, successive overshoots occur, generating the observed oscillatory behavior. By analogy, one can think of a simple dynamical system which admits a stable steady solution at low A before undergoing a supercritical Hopf bifurcation at $A = A_H$ to produce stable oscillations while the steady solution has become unstable. The variable in which the solution oscillates, the iteration number, is discrete which may account for the small departures from strictly periodic oscillations that can be observed in the data (figures 3(b)–(d)), as the period may vary continuously with A.

We look for ECS that are stationary, and so seek solutions with λ_c close to zero. Figure 4 shows the largest real eigenvalue after 50 iterations λ_{50} for values of A spanning the interval $[5, 8]$. Although our results have been checked using a refined mesh (64×64 modes) and the leading eigenvalue converged to 10^{-4} in most cases, we emphasize that convergence is not required at this stage as this algorithm is only intended to provide a good initial condition for a Newton iteration. The results reveal two possible candidates, corresponding to values of λ_{50} close to 0: $A_1 \approx 6.55$ and $A_2 = A_H \approx 6.81$. The state corresponding to A_1 is

undoubtedly a good initial condition as $\lambda_{50} < 0$ for $A < A_1$ and $\lambda_{50} > 0$ for $A_2 > A > A_1$. That corresponding to A_2 is seemingly less secure: for $A = 6.81$, the converged eigenvalue is $\lambda_c(A = 6.81) \approx 0.003191$ and approaches 0 from above as A is increased but the oscillatory regime is reached by $A = 6.82$ leading to small amplitude oscillations close to but not crossing zero.

These impressions can be confirmed by inserting the approximate solution with amplitude A_1 into the Newton algorithm described in Sec. III B. On a 32×64 meshgrid the solution readily converges to a lower branch state at this Reynolds number ($\mathrm{Re} = 400$). In contrast, when the solution with amplitude A_2 is used the solution converges to the corresponding upper branch state.

B. Continuation in Reynolds number

The regularized equations (37)–(40) contain the parameter $\epsilon \equiv 1/\mathrm{Re}$. The presence of this parameter allows us to continue the solutions obtained above to both larger and smaller Reynolds numbers. The results for a 32×64 meshgrid are displayed in figures 5 and 6.

The solution branches are plotted in six different ways. In figure 5(a) we present $N_u \equiv 2E_u$, where $E_u \equiv \frac{1}{2D}\int_{\mathcal{D}} u_0^2(y,z)\,dy\,dz$ is the streamwise-invariant streamwise kinetic energy per unit volume and $D \equiv \int_{\mathcal{D}} dy\,dz$. In figure 5(b) we present $N_\omega \equiv 2\,\mathrm{Re}^2\,E_\omega \equiv \frac{1}{D}\int_{\mathcal{D}} \omega_1^2(y,z)\,dy\,dz$, a quantity related to the streamwise-invariant in-plane enstrophy per unit volume. In figure 5(c) we present the quantity $N' \equiv 2\mathrm{Re}^2 E'$, where $E' \equiv \frac{1}{2D\,\mathrm{Re}^2}\int_{\mathcal{D}}(v_1^2 + w_1^2)\,dy\,dz$ measures the streamwise-fluctuating in-plane kinetic energy per unit volume. The lower branch (labeled L) passes a saddle-node at $\mathrm{Re} \approx 136$, giving rise to an upper branch (labeled U). Figure 6 shows a projection of our solutions onto pointwise maxima of the corresponding quantities, thereby providing a complementary representation of the results.

The emergence of the upper branch is rather unexpected since the reduced system (37)–(40) was developed by appealing to lower branch scalings. Evidently the asymptotic procedure is sufficiently robust to capture both lower *and* upper solution branches. However, the computation of the upper branch is more delicate. As observed by Beaume *et al.* [21], upper branch solutions and their critical layer have a different spatial structure which dramatically increases the computational cost. To continue these solutions we used a 64×128 meshgrid and adjusted the preconditioner as necessary. Specifically, we started by testing a few values of $\triangle t$ (see Sec. III B) and selected the most efficient one for continuation near the saddle-node. We then continued the upper branch until the algorithm failed. Each time this occurred we tested a few values of $\triangle t$ to determine the most suitable one, repeating this process as many times as necessary to continue the branch up to the desired value of the Reynolds number. Upper branch solutions can also be computed directly by starting from the approximate solution with amplitude A_2, obtained using the iterative scheme of Sec. III A, and applying the Newton algorithm with the modified preconditioner described above. In particular, the upper branch is identified with the value of $A \approx 7.04$ at which the (unstable) fixed point of the iterative process corresponds to zero eigenvalue.

Some care is required in interpreting the values of the energies in figure 5, as N_ω and N' are proportional to Re^2. The trivial solution, for which $N_u = 1$, $N_\omega = N' = 0$, represents

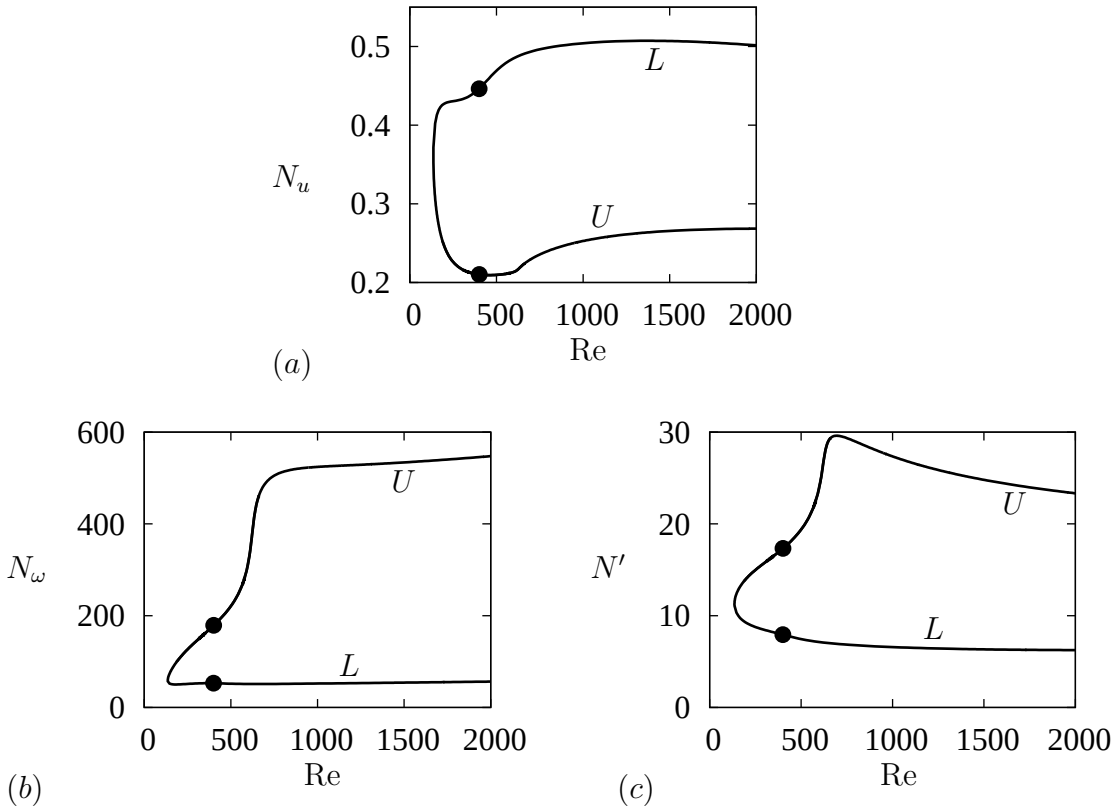

FIG. 5. Bifurcation diagrams showing branches of exact coherent states as a function of the Reynolds number Re obtained by continuation of converged solutions (solid dots) starting from approximates generated by the iterative algorithm with initial amplitude A_1 (converged to a lower branch state, indicated by L) and A_2 (converged to an upper branch state, indicated by U). (a) N_u, (b) N_ω, (c) N'.

the state of maximal transport and hence has the greatest kinetic energy. All other ECS are found to have a lower kinetic energy, as indicated by lower values of N_u. The quantities N_ω and N', as well as the maximum of ω_1 and the amplitude A, remain $O(1)$ along the lower branch, reflecting the relevance of the reduced model. Interestingly, a similar observation can be made for the upper branch solution for which the fluctuations also remain $O(1)$. However, possible departures from the assumed scaling may be observed in the enstrophy-related norm of the upper branch states. Indeed $N_\omega = O(100)$, $\max(\omega_1) \sim 80 - 90$ at $\mathrm{Re} = O(1000)$, suggesting that the vorticity becomes larger and larger in an increasingly narrow region. However, these values, despite being relatively large at low Re do not appear to increase sufficiently with Re to violate the assumed ordering in the expansion.

Figure 7 depicts the lower branch solution at $\mathrm{Re} \approx 1500$ using streamwise-averaged quantities while figure 8 provides a three-dimensional rendition of this solution. Figures 9 and 10 provide analogous representations of the upper branch solution at the same Reynolds number. The lower branch solution possesses a smoothly undulating critical layer that is maintained by two nearly circular rolls (cf figure 7(a)). This structure is supported by fluc-

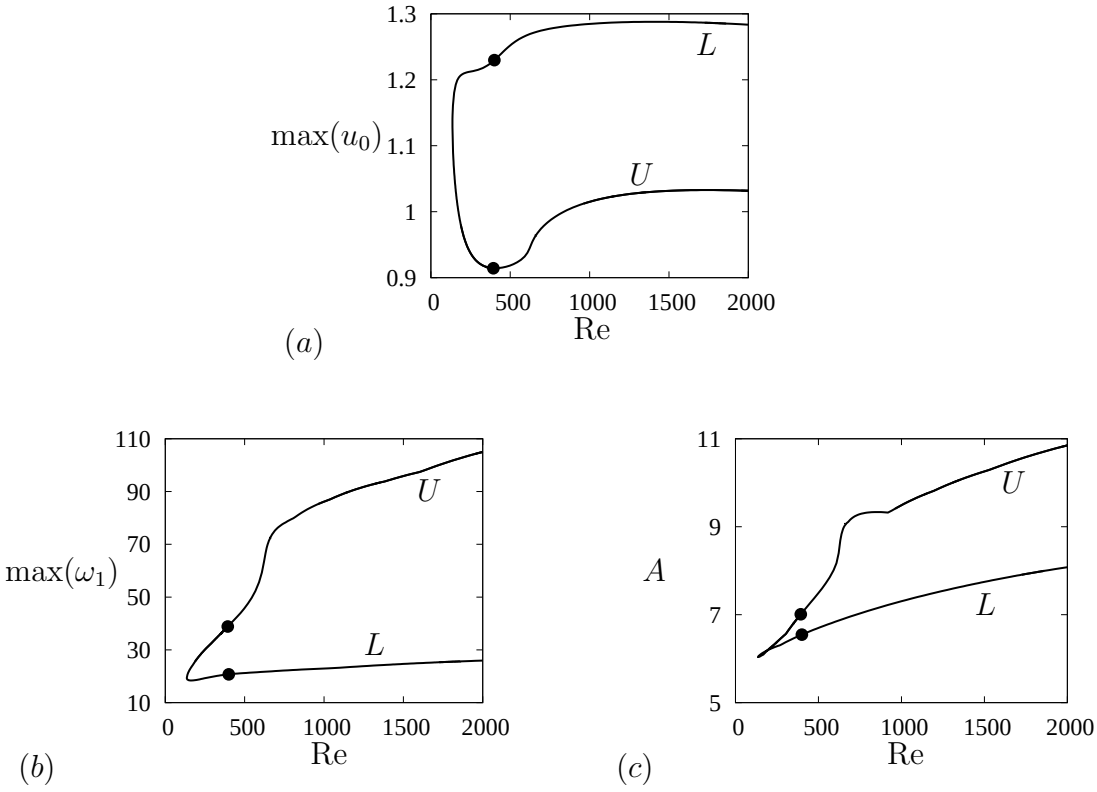

FIG. 6. The same bifurcation diagrams as in figure 5 rendered in terms of the maximum values of (a) the streamwise velocity u_0, (b) the vorticity ω_1 and (c) the amplitude A of the self-consistent fluctuation field.

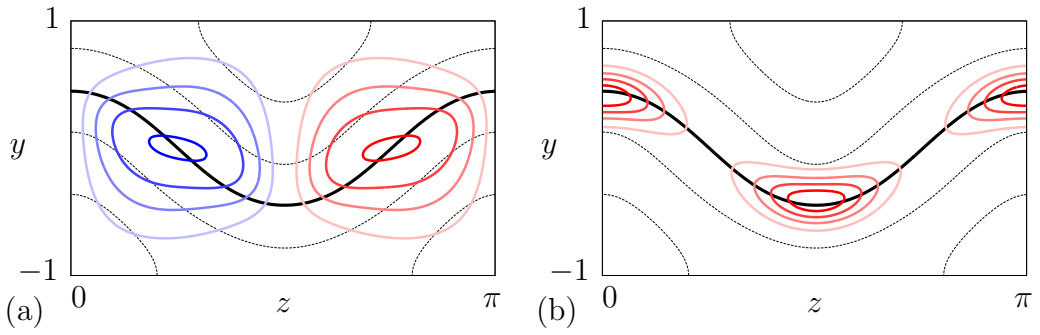

FIG. 7. (Color online) Lower branch solution computed at Re ≈ 1500 represented by (a) contours of the streamwise-constant streamfunction ϕ_1 and (b) contours of $|(v_1, w_1)|_{L_2}$ representing the amplitude of the in-plane fluctuations. Positive streamwise contours are shown in red (right roll) while negative contours are shown in blue (left roll); contours are equidistributed to give a sense of local gradients. Each contour plot is overlaid on the streak profile shown in black, with the solid line representing the critical layer $u_0 = 0$. Three-dimensional visualizations of the fluctuating variables are displayed in figure 8.

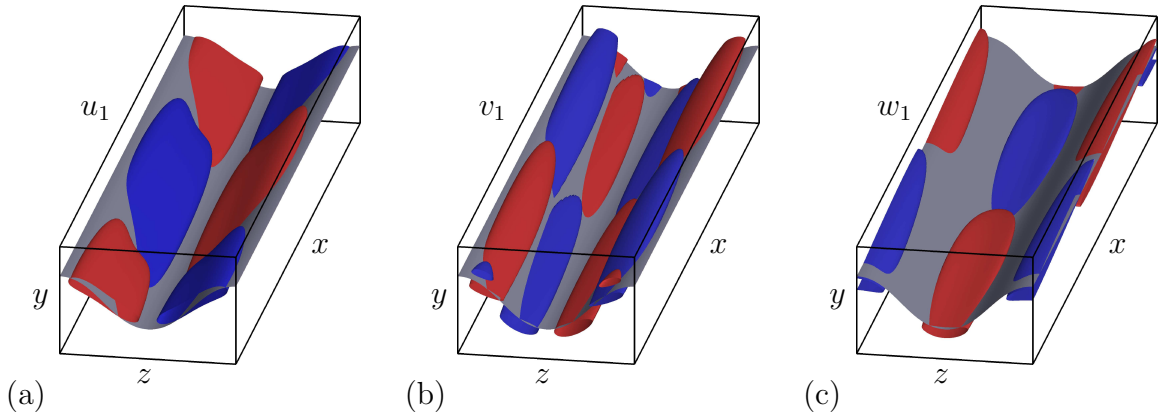

FIG. 8. (Color online) Three-dimensional rendition of the fluctuating flow associated with the lower branch solution at Re ≈ 1500. The surfaces represented in color correspond to two equal and opposite values at half the maximum value of (a) the streamwise-fluctuating streamwise velocity u_1 , (b) the streamwise fluctuating wall-normal velocity v_1, and (c) the streamwise-fluctuating spanwise velocity w_1. Red (light gray) color corresponds to positive values while blue (dark gray) corresponds to negative values. The gray surface shows the critical layer $u_0 = 0$.

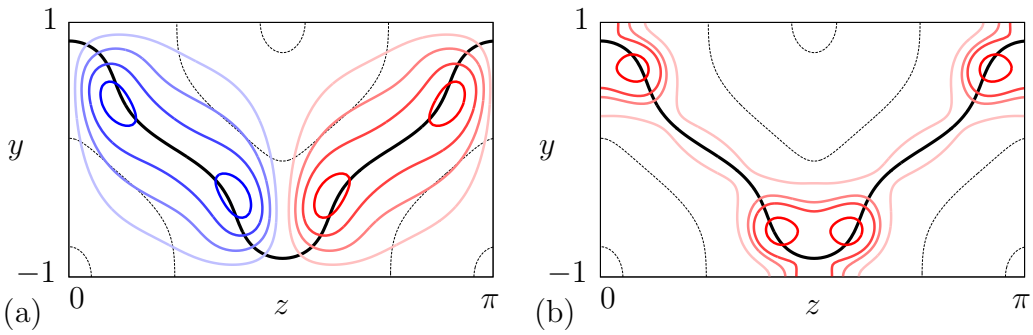

FIG. 9. (Color online) Same representation as in figure 7 but for the upper branch solution at Re $\approx$ 1500. Three-dimensional visualizations of the fluctuating variables for this solution are displayed in figure 10.

tuations accumulating in the critical layer. Figure 7(b) shows that these fluctuations have a rapid variation in the direction perpendicular to the critical layer (its thickness being proportional to $(\alpha \mathrm{Re})^{-1/3}$) while slow variations are observed *along* the critical layer. The three-dimensional representations in figure 8 confirm these observations and shed some additional light on the streamwise dynamics of the lower branch solution. The streamwise-fluctuating streamwise velocity u_1 is essentially concentrated in the regions of stronger streamwise-invariant streamfunction ϕ_1 (compare figure 7(a) with figure 8(a)) and therefore away from the crests of the critical layer. As a consequence of the incompressibility of the fluctuations (Eq. 34), the in-plane fluctuating dynamics accumulate at the extrema of the critical layer, away from the location of the streamwise rolls, as documented in figure 7(b). Figure 8 shows that at $x = 0$ (defined arbitrarily as the front section in the figure), in the region around

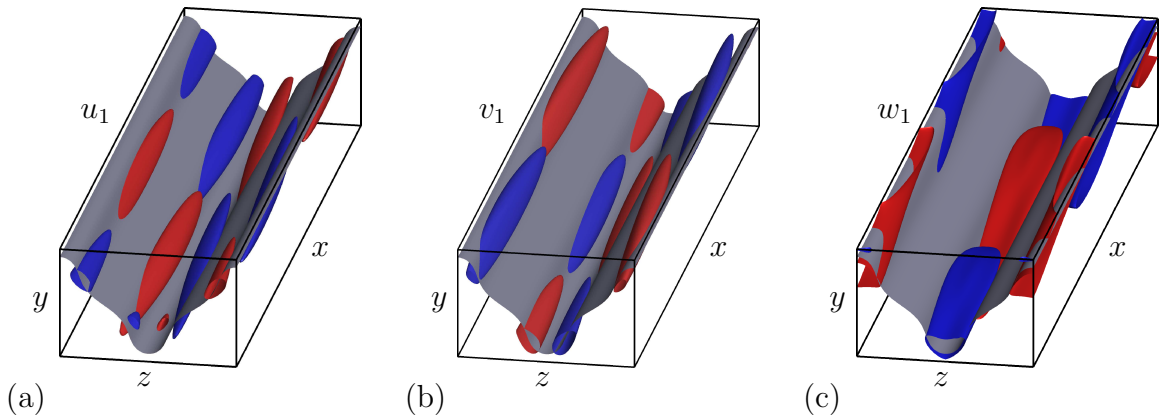

FIG. 10. (Color online) Same representation as in figure 8 but for the upper branch solution at Re ≈ 1500. Intersections of non-zero fluctuations with the upper and lower walls can be observed in (c) and are allowed by the stress-free boundary conditions.

the lowest point of the critical layer, $z = \pi/2$, the fluid flows from left to right along the $u_0 = 0$ surface. The reverse occurs half a period downstream and at the highest point of the critical layer (located at the boundary of the (periodic) domain when $x = 0$).

In comparison to the lower branch solution, the upper branch solution has stronger variations along the critical layer, the extrema of which approach the top and bottom walls. This change in shape is a signature of stronger rolls. The resulting structure is shown in figure 9(a), where by comparison with figure 7(a), it is evident that the rolls are stretched diagonally and split, displaying a bimodal structure. This last feature is responsible for the sharper crests of the $u_0 = 0$ surface relative to that for the lower branch solution. This change in structure is reminiscent of the differences between lower and upper branch states in PCF (see figure 7 from [53]) and hints at the usefulness of our reduced model for states beyond the lower branch states for which it was developed. Associated with the bimodal structure in ϕ_1 is a similar bimodal structure of the fluctuations which are now strongly localized on either side of the critical layer turning points. Figure 9 shows that as a result the location of the streamwise rolls almost coincides with the maxima of the fluctuation field, suggesting that the increased shear in the streamwise rolls suppresses fluctuations, with the location of the self-sustaining process moving towards the critical layer turning points. This evolution in turn implies that for the upper branch states the width of the critical layer depends strongly on location along the critical layer: the layer appears broader near its maximum deflection from $y = 0$ and is substantially thinner in the intervals inbetween. In addition, the amplitude of both the rolls and the spanwise fluctuations peaks strongly in the vicinity of these turning points. Although we have not pursued this phenomenology further, the results suggest that in the limit Re $\to \infty$ the common assumption of uniform critical layer thickness may require reexamination, with the critical layer "breaking up" into something more akin to critical "spots", where most of the critical layer forcing is concentrated (figure 9(b)).

These properties of the lower and upper branch solutions are reflected in the associated mean streamwise velocity profiles shown in figure 11. As expected, the ECS in each case

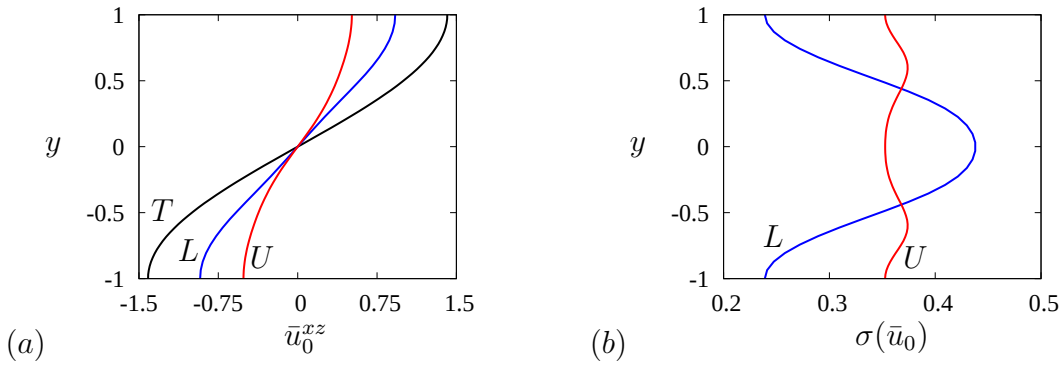

FIG. 11. (Color online) Streamwise velocity profiles at Re ≈ 1500. (a) (x,z)-averaged streamwise velocity $\bar{u}_0^{xz}$ as a function of the wall-normal coordinate y. (b) Standard deviation $\sigma(\bar{u}_0)$ of the streamwise velocity u_0 from $\bar{u}_0^{xz}(y)$. The trivial solution is shown in black (labelled T), the lower branch (labelled L) in blue and the upper branch (labelled U) in red.

reduces the shear across the layer. The reduction is less for the weaker lower branch ECS than for the upper branch ECS (figure 11(a)). Of particular interest is the standard deviation of the velocity from these profiles, $\sigma(\bar{u}_0, y) = \sqrt{\int_z (u_0(y,z) - \bar{u}_0^{xz})^2 dz}$, shown in figure 11(b). For the lower branch ECS σ peaks at mid-height where the streamwise rolls are strongest and falls off quite strongly towards the walls at $y = \pm 1$ (figure 11(b)). In contrast, on the upper branch σ is quite uniform across the layer, with a local minimum at mid-height, an effect that can be directly attributed to the stretching of the streamwise rolls along the critical layer and the location of their peak amplitude near regions of maximum deviation of the critical layer from $y = 0$.

C. Spectra

To check the accuracy of the solutions, we plot in figure 12 the one-dimensional spectra of the fluctuation velocity in the wall-normal and spanwise directions. These are defined in terms of the normalized partial sums

$$\Sigma_y(m_y) = \frac{1}{2(M-1)N} \left(S^2(m_y,0) + \sum_{m_z=1}^{N} (S^2(m_y,m_z) + S^2(m_y,-m_z)) \right)^{1/2}, \tag{49}$$

$$\Sigma_z(m_z) = \frac{1}{2(M-1)N} \left(\sum_{m_y=0}^{M} S^2(m_y,m_z) \right)^{1/2}, \tag{50}$$

where $S^2(m_y,m_z) = |v_1(m_y,m_z)|^2 + |w_1(m_y,m_z)|^2$ and M (resp. N) is the maximum wave number in the y (resp. z) direction. The quantity $\Sigma_y(m_y)$ (resp. $\Sigma_z(m_z)$) has been defined in such a way thay it is proportional to the sum of the amplitudes of the fluctuations with wave number m_y (resp. m_z) in the y (resp. z) direction. The plots confirm that the amplitude of the upper branch fluctuations is larger than that along the lower branch solutions. In addition, the spectra in the wall-normal direction decay exponentially at the same rate for both lower and upper branch states while the spectrum of the upper branch solution decays

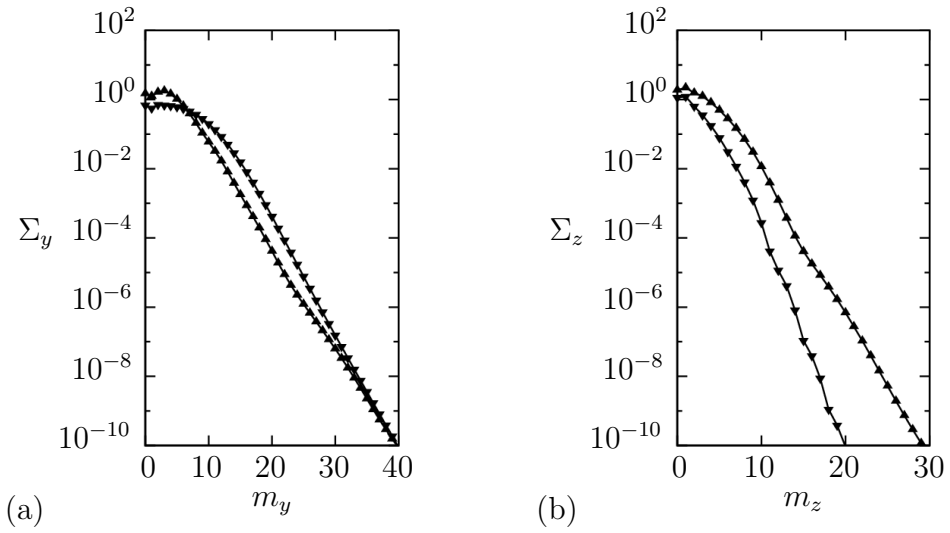

FIG. 12. Spectra of the lower (downward triangles) and upper (upward triangles) branch solutions represented through the normalized partial sums $\sum_y(m_y)$ and $\sum_z(m_z)$ defined in Eqs. (4.2) and (4.3).

more slowly in the spanwise direction than that of the lower branch solution. These results reflect the fact that the scales of the wall-normal variation remains comparable as one goes from the lower branch to the upper one while the smallest spanwise scale shrinks. These results highlight the fact that the change in structure between the lower and upper branches is primarily associated with differences in the spanwise variation of the fields and inform the numerical requirements to compute these solutions accurately: while the wall-normal mesh can be designed independently of the solution sought with 30 wave lengths sufficient at $\mathrm{Re} = 1500$ (i.e., approximately 30 modes in the cosine/sine basis, or 60 modes in the complex Fourier basis), the number of points in the spanwise direction needs to be increased by a factor of about 1.5 for upper branch states at $\mathrm{Re} = 1500$. Obviously, increasing the Reynolds number or any other factor that sharpens the critical layer impacts these requirements.

D. ECS dependence on the domain size

We next investigate how the solutions computed in the previous section depend on the spanwise domain size L_z and the imposed streamwise wave number $\alpha = 2\pi/L_x$. We begin by fixing $\alpha = 0.5$ and studying the effect of varying L_z. The resulting bifurcation diagrams are shown in figure 13. Continuation of the lower branch states to domains with smaller spanwise extent reveals that they pass a saddle-node at $L_z \approx 2.1$ before terminating on a branch of solutions with two wave lengths per period when $L_z \approx 2.5$. These solutions are depicted in the top two panels in figure 14 together with the initial lower branch solution at $L_z = \pi$ in the third panel. The rolls present at $L_z = \pi$ gradually tilt as the domain period is reduced (figure 14, second panel). Beyond the saddle-node at $L_z \approx 2.1$ these tilted vortices continue to stretch diagonally, in a direction transverse to the critical layer. As this

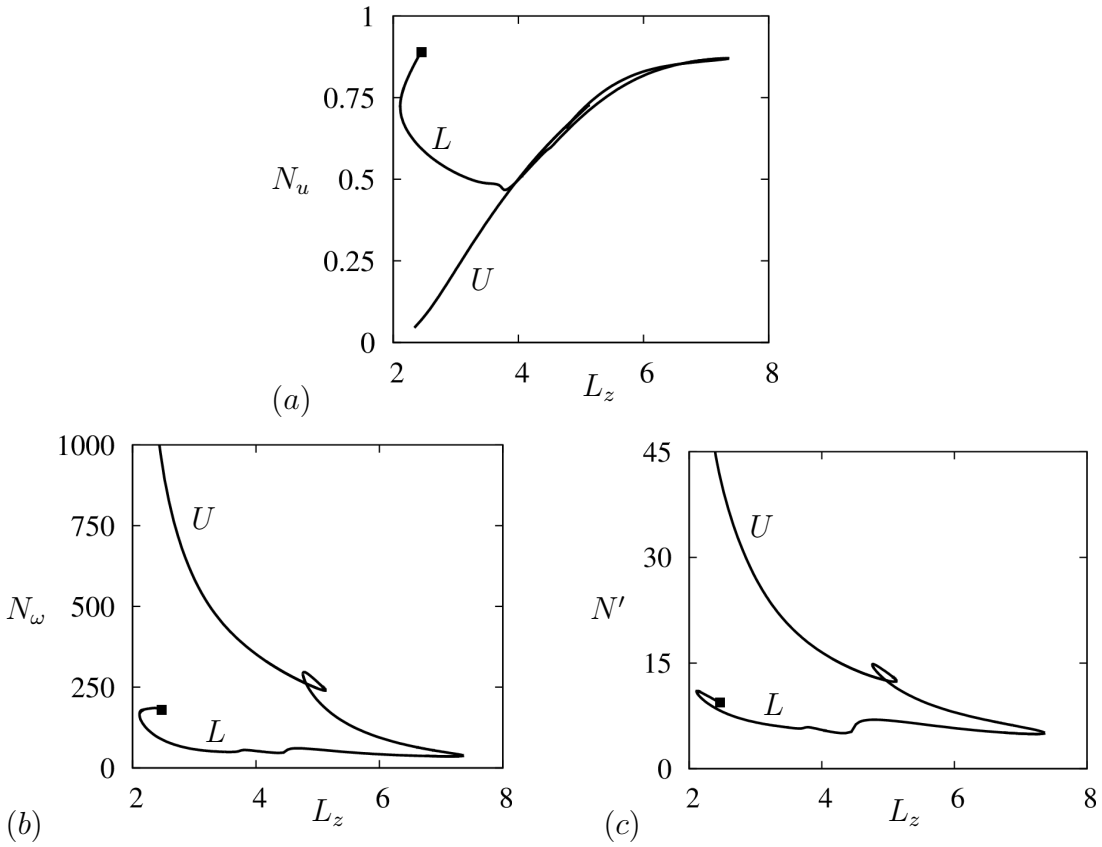

FIG. 13. The ECS at Re ≈ 1500 as a function of the spanwise period L_z. The diagrams show (a) N_u, (b) N_ω (c) and N'. The full square indicates the termination of the branch on a branch of solutions with two wave lengths in the domain (figure 14, upper panel). Solutions along the lower branch (denoted by L) are shown in figure 14, while those on the upper branch (denoted by U) are shown in figure 15.

happens the centre of each roll gradually splits forming two co-rotating rolls, one on either side of the critical layer, a process that greatly reduces the deflection of the critical layer from its laminar location at $y = 0$. At the same time small counter-rotating rolls appear in the corners above and below each tilted structure and these grow in strength as L_z increases, ultimately forming a period two state at $L_z \approx 2.5$ with an unperturbed $y = 0$ critical layer (figure 14, top panel). The resulting period-doubled ECS bears a number of similarities with the solutions EQ7 and EQ8 first observed by Gibson *et al.* [3] and reported in figure 16 of Gibson & Brand [54].

Continuing the lower branch state at $L_z = \pi$ in the opposite direction, towards larger L_z, reveals a new type of behavior. The increasing domain size stretches the rolls, which evolve into a bimodal structure reminiscent of the upper branch solution with $L_z = \pi$ (compare figure 14, fourth panel, with figure 9(a)). Increasing L_z further leads to the progressive breakup of each of the original rolls into a pair of co-rotating rolls (figure 14, fourth panel). Once formed these rolls are pulled farther apart as L_z increases, resulting in a periodic array of pairs of counter-rotating rolls supporting a highly deformed critical layer interspersed with

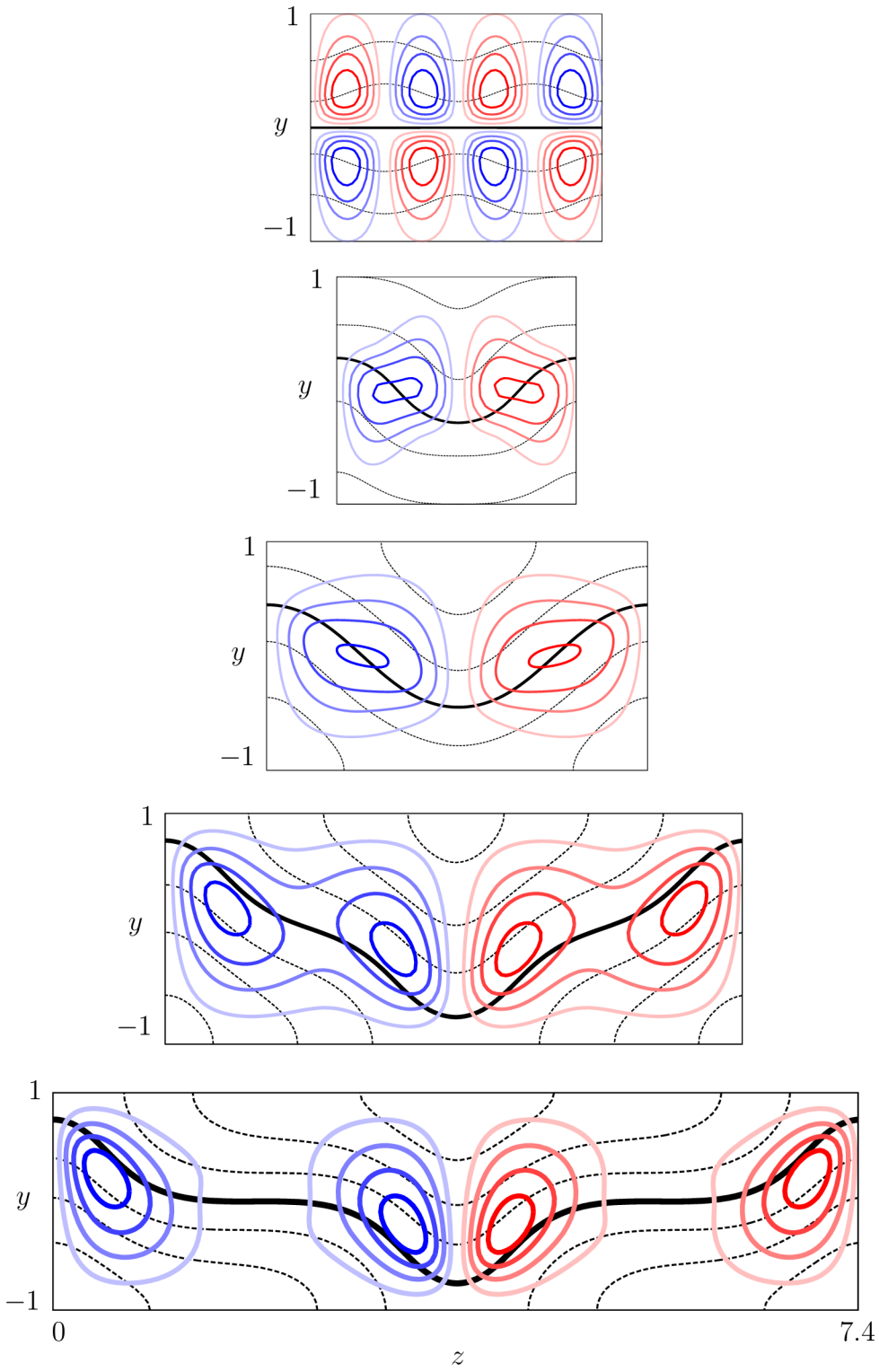

FIG. 14. (Color online) Structure of the lower branch solutions with different spanwise periods L_z represented in the same way as in figure 7. From top to bottom: endpoint of the branch at $L_z \approx 2.5$, left saddle-node at $L_z \approx 2.1$, solution at $L_z = \pi$ (taken from figure 7), solution at $L_z \approx 5$ and solution at the right saddle-node at $L_z \approx 7.4$. The contour values of the streamwise velocity are the same throughout, but different values of the streamfunction are used from panel to panel for better representation of the flow. The contours are in all cases equidistributed and the scale of the domain is kept the same for all solutions.

connecting zones where the trivial laminar flow is only weakly perturbed (figure 14, bottom panel). The resulting state cannot be continued to larger domain sizes and passes a saddle-node at $L_z \approx 7.4$ where it connects with states originating along the upper branch (see below and figure 15). This type of behavior is similar to that observed for PCF by Deguchi *et al.* [55] but is not related to spatial localization in the spanwise direction as conventionally understood, since true localized states must become independent of the domain size.

From the saddle-node solution (last panels in figures 14 and 15) one can continue the branch back to lower values of L_z but in the direction of increasing fluctuation intensity, i.e., along the upper branch (see figure 13(c)). The resulting upper branch states are shown in figure 15. As the period L_z is reduced from $L_z \approx 7.4$ along the upper branch the stretching gradually disappears, but the co-rotating rolls do not merge, in contrast to the behavior along the lower branch. Instead, two additional rolls are nucleated between the orginal pair of co-rotating rolls, and these also co-rotate (figure 15, fourth panel). The net result is an array of four co-rotating rolls whose combined action deforms the critical layer further from the laminar case, and these are paired with a similar set of four co-rotating rolls in the other half of the domain, but rotating in the opposite sense. This four-roll structure is destroyed as the branch passes through a loop between $L_z \approx 4.8$ and $L_z \approx 5.1$: the two weaker middle rolls that have appeared along the upper branch below $L_z \approx 7.4$ gradually fade, thereby restoring the bimodal structure (figure 15, second panel) and generating the state in figure 9. When L_z is decreased further, the bimodal structure gradually disappears as the rolls are squeezed together (figure 15, top panel). At the same time, both the mean streamfunction and the fluctuation fields grow without bound while the streamwise velocity u_0 becomes increasingly homogenized and ultimately approaches zero. These developments are reflected in the dramatic decrease in the streamwise velocity norm N_u, together with increases in enstrophy norm N_ω and fluctuation norm N' shown in figure 13, and indicate that the postulated form of the solutions is starting to break down. Thus solutions in this regime are unlikely to be physically relevant.

We mention that in related calculations for PCF, Melnikov *et al.* [56] find that the lower and upper branch states form an isola in L_z with no additional bifurcations (except for saddle-nodes) as L_z varies.

We have also studied how the morphology of the ECS in a domain with $L_z = \pi$ varies at fixed $\mathrm{Re} = 1500$ when the streamwise wave number α is changed. The bifurcation diagrams obtained are shown in figure 16. The figure reveals that the ECS lie on an isola and therefore do not connect to any other solution. Thus the isola defines an interval of existence for the ECS at $L_z = \pi$ and $\mathrm{Re} = 1500$: $0.0380 < \alpha < 1.1890$. While the lower bound for α hints at the persistence of these structures for very long domains ($L_x \approx 165$), the upper bound indicates that the required streamwise periodicity of the domain be at least $L_x \approx 5.3$ for these structures to be self-sustaining, a value close to that observed in PCF [13]. The ECS at the left and right saddle-nodes along the isola are represented in figure 17. For small α (long streamwise domain), the critical layer is distorted approximately sinusoidally by nearly circular rolls and the fluctuations do not exhibit sharp gradients despite being located close to the critical layer $u_0 = 0$. In contrast, for large α and therefore short streamwise domains, the fluctuations become very localized and the associated critical layer

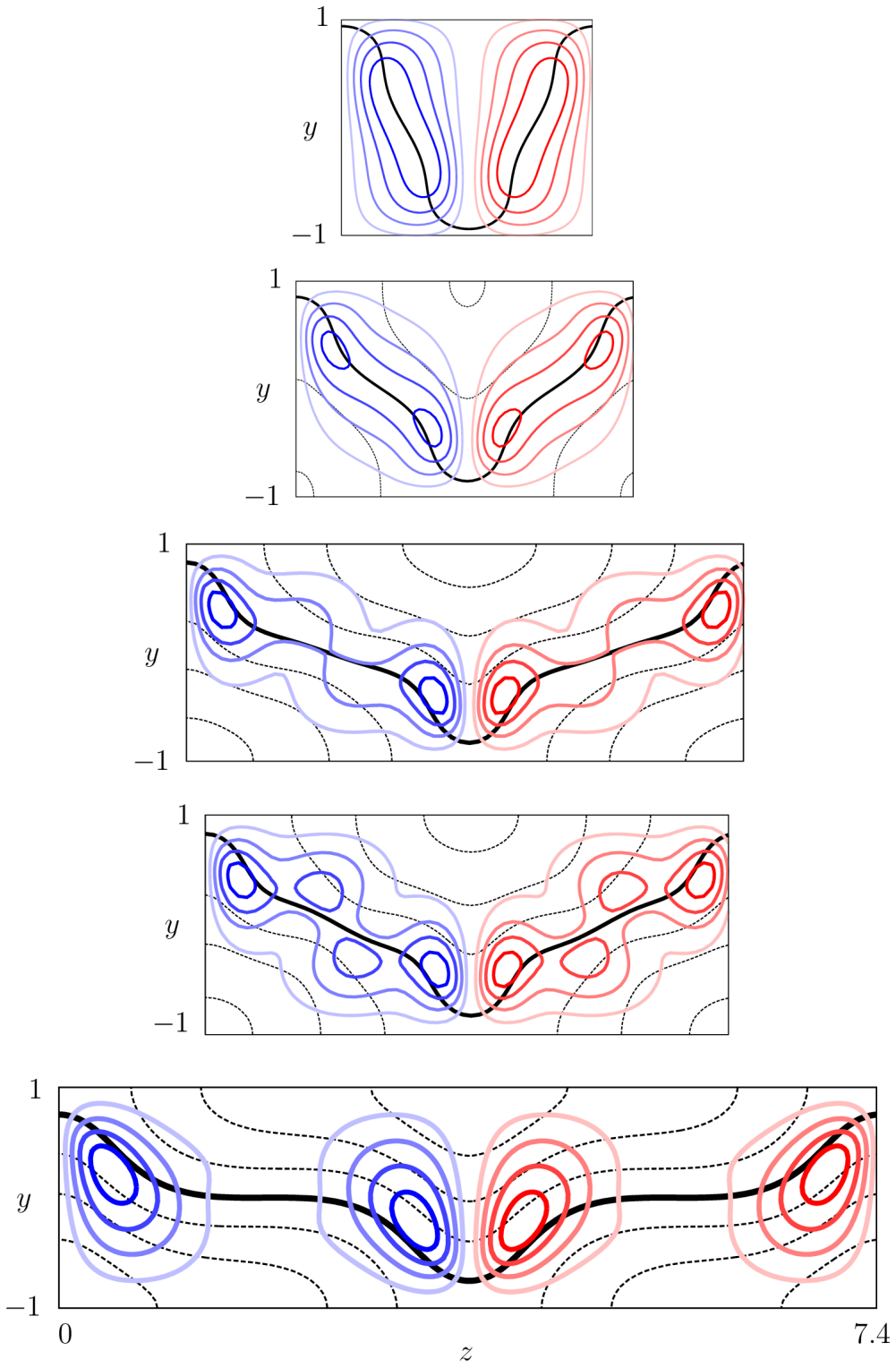

FIG. 15. (Color online) Structure of the upper branch solutions with different spanwise periods L_z. From top to bottom: diverging solution at $L_z \approx 2.3$, solution at $L_z = \pi$ (taken from figure 9), solution at the right saddle-node of the loop at $L_z \approx 5.1$, solution at the left saddle-node of the loop at $L_z \approx 4.8$ and solution at the right saddle-node at $L_z \approx 7.4$ (taken from figure 14). The same figure style is used as for figure 14.

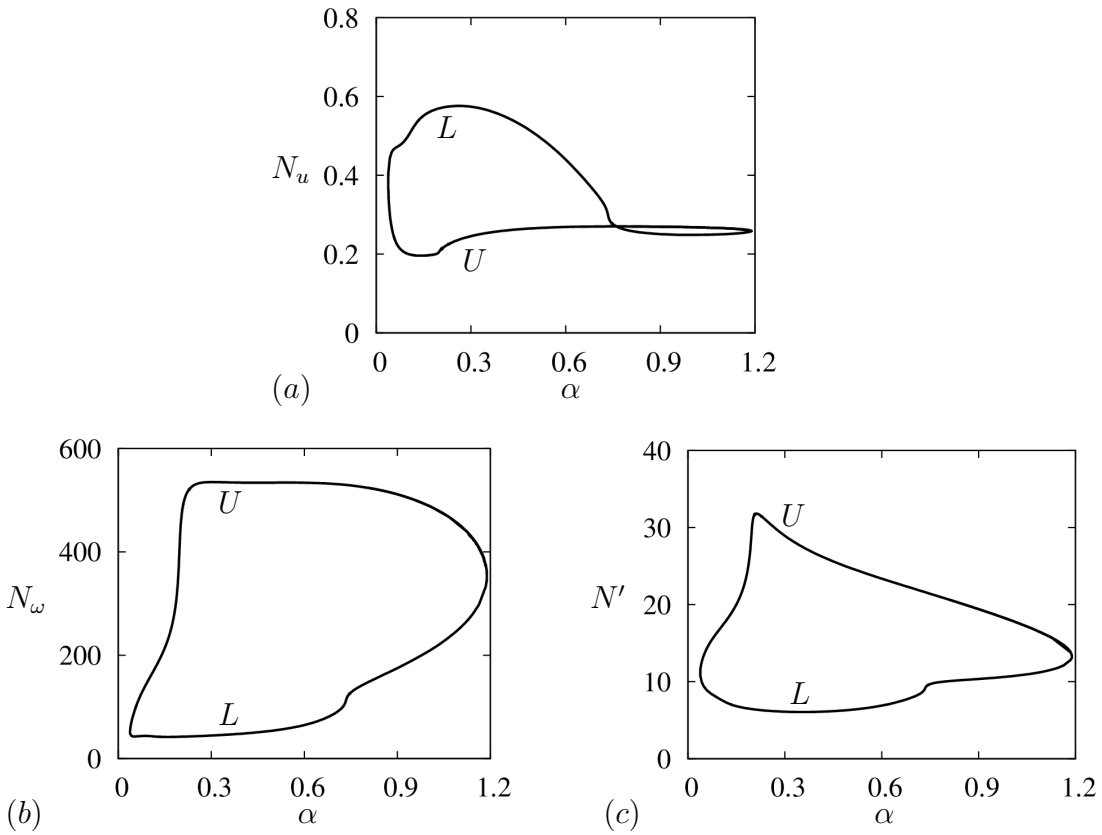

FIG. 16. Bifurcation diagrams showing the ECS at Re = 1500 and $L_z = \pi$ as a function of the streamwise wave number α. (a) N_u. (b) N_ω. (c) N'. Solutions at the left and right saddle-nodes are shown in figure 17. The letter L (resp. U) denotes the lower (resp. upper) branch.

is deformed into a sawtooth profile. The associated rolls are highly elongated and align with the approximately constant slope sections of the critical layer. These developments are a consequence of the $(\alpha \mathrm{Re})^{-1/3}$ critical layer scaling [57]. As Re is kept fixed, decreasing α increases the width of the critical layer thereby weakening the strength of the fluctuations. This is a direct consequence of the fact that α affects the amplitude of the u_0-induced advection of fluctuations, as described by Eq. (40). As a result decreasing the value of α decreases the coupling between the mean and fluctuation fields. Thus, the fluctuations no longer track the critical layer efficiently, and so remain weak and do not deform the rolls. The associated critical layer is sinusoidal. The converse is true when α is increased: the coupling becomes stronger, leading to fluctuations that are strongly focused on the critical layer and that substantially deform the rolls and hence generate a strongly distorted critical layer.

V. DISCUSSION

In this paper we have presented a simple rational procedure that leads to a reduced description of plane parallel shear flows. The method assumes that the flow is dominated by

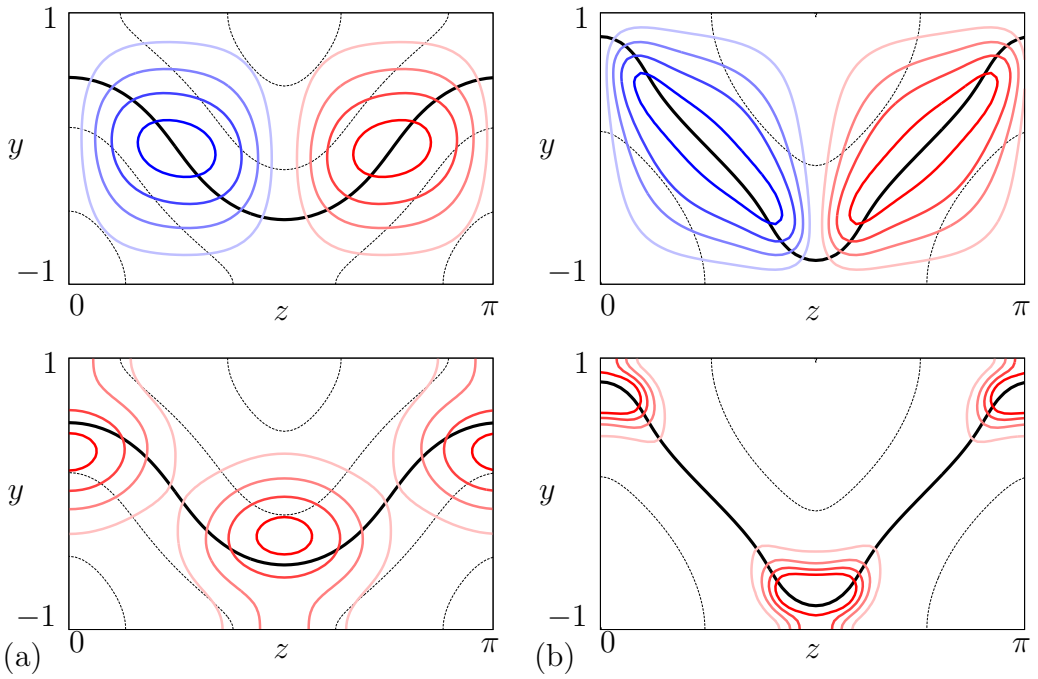

FIG. 17. (Color online) Structure of the ECS at (a) the left saddle-node at $\alpha \approx 0.0380$ ($L_x \approx 165$) and (b) the right saddle-node at $\alpha \approx 1.1890$ ($L_x \approx 5.3$) of the isola shown in figure 16. The solutions are represented through their mean streamwise velocity with contours of the streamfunction (top panel) and the fluctuation norm (bottom panel). The contours are in all cases equidistributed.

the mean streamwise flow component, with spanwise components of the velocity field (the rolls) that are much weaker. Despite this the Reynolds stress generated by the fluctuating fields modifies the mean spanwise velocity and hence the mean streamwise flow, as described by Eqs. (29)–(31), and this in turn modifies the fluctuations as described by Eqs. (32)–(34). Of these the former are simplified in having an $O(1)$ effective Reynolds number while the latter constitute a viscously regularized (cf. [14, 17]) but quasilinear system that admits solutions of arbitrary amplitude. In our approach this amplitude is determined by a self-consistency requirement: in steady state the Reynolds stress generated by the fluctuations must be such as to produce a streamwise flow for which the fluctuations neither grow nor decay, and we have described an iterative process whereby the amplitude of the fluctuations can be adjusted to realize this requirement. Our approach therefore captures the essence of the self-sustaining mechanism identified by Waleffe [2] and leads to reduced equations that capture the universality in the behavior of plane parallel shear flows. We believe that these equations are suitable not only for studying steady ECS with critical layers but also exact traveling waves and indeed other nonequilibrium structures with no critical layer at all. In this respect the equations possess advantage over detailed studies of particular flows using flow-specific scalings. However, to justify these claims our results for WF and other flows will have to be compared quantitatively with solutions of the corresponding fully three-dimensional problems. In addition, such comparisons will determine, on a case by case basis, the range of Reynolds numbers for which our results provide a reliable guide to the solutions

of the full problem.

We have applied the numerical algorithm developed here to compute a variety of exact coherent states in a body-force driven flow we refer to as Waleffe flow. The fundamental assumptions we make turn out to capture not only the expected lower branch states but also the corresponding upper branch states, reached via numerical continuation in the parameter $\mathrm{Re} \equiv 1/\epsilon$. The results we obtain are similar to the corresponding PCF results obtained by Blackburn *et al.* [14] for lower branch states and by Deguchi *et al.* [58] for upper branch states via continuation in L_z. This fact is significant since there is no guarantee that continuation in L_z will identify the same states as continuation in Re. In both systems the lower branch critical layer deforms into a sinusoidal surface through the action of the rolls, while the deformation corresponding to the upper branch states is both stronger and bimodal. Particularly intriguing is our discovery that along the upper branch the width of the critical layer is no longer uniform and that the bimodal structure of the rolls and streaks concentrates the critical layer forcing in regions of maximum departure from the unperturbed critical layer. Current asymptotic approaches do not take this possibility into account. However, the intrinsic self-consistency of our reduced equations implies that this new critical layer structure is likely a property of upper branch states in the full system at large Re.

We have also used numerical continuation to continue our solutions in the spanwise domain length L_z and in the streamwise wave number α. The former determines the existence region for the solutions we have found and shows that the lower branch solutions at small L_z bifurcate from a period two spatially periodic state but undergo a saddle-node bifurcation at larger L_z that connects the lower and upper branch states. The solutions near this fold are stretched in the spanwise direction relative to $O(1)$ domains but are not spatially localized in the conventional sense, in contrast to the suggestion made by Deguchi *et al.* [55], since they cannot be continued to larger L_z and hence to larger separations. The continuation in the streamwise wave number α leads to simpler results – this time the lower and upper branch states are connected by folds at either end and the solutions lie on an isola. As a result they do not extend to either very small or very large values of α. We believe that these states, as well as those obtained via continuation in Re, will prove of great value in further explorations of the full set of reduced equations, including studies of spatial modulation and possible localization in the streamwise direction. We hope to report on these explorations in a future publication.

The approach described here has been used with considerable success to derive reduced descriptions of other strongly anisotropic flows, including convection in a strong magnetic field [35] and rapidly rotating convection [59–61]. In all these cases the mean field adjusts on a slower timescale than the timescale on which the fluctuations evolve. As a result the mean flow can be taken to be quasistatic and the fluctuations can be computed at fixed values of this field. The mean can then be updated based on the fluctuations computed on this basis, and the process repeated. Alternatively the reduced system can be treated as a dynamically coupled system for the fluctuations and the mean, and the combined system time-stepped together. The latter procedure has been used successfully in the context of rapidly rotating convection [59–61] and we anticipate that time-stepping Eqs. (29)–(34) for transition values

of the Reynolds number could lead to similar insights. This, too, is a topic for future study.

ACKNOWLEDGMENTS

CB acknowledges support from the Geophysical Fluid Dynamics Program at the Woods Hole Oceanographic Institution for his 2012 fellowship where the first results were obtained. The work was supported by the National Science Foundation under grants DMS-1211953 and DMS-1317596 (CB & EK), OCE-0934827 (GPC) and OCE-0934737 and DMS-1317666 (KJ). E.K. wishes to acknowledge additional support from the Chaire d'Excellence Pierre de Fermat de la région Midi-Pyrénées (France).

---

[1] M. Nagata, J. Fluid Mech. **217**, 519 (1990).
[2] F. Waleffe, Phys. Fluids **9**, 883 (1997).
[3] J. F. Gibson, J. Halcrow, and P. Cvitanović, J. Fluid Mech. **611**, 107 (2008).
[4] H. Faisst and B. Eckhardt, Phys. Rev. Lett. **91**, 224502 (2003).
[5] H. Wedin and R. R. Kerswell, J. Fluid Mech. **508**, 333 (2004).
[6] Y. Duguet, A. P. Willis, and R. R. Kerswell, J. Fluid Mech. **613**, 255 (2008).
[7] Y. Duguet, A. P. Willis, and R. R. Kerswell, J. Fluid Mech. **663**, 180 (2010).
[8] A. Schmiegel, *Transition to turbulence in linearly stable shear flows*, Ph.D. thesis, Marburg University (1999).
[9] F. Waleffe, J. Fluid Mech. **435**, 93 (2001).
[10] G. Kawahara and S. Kida, J. Fluid Mech. **449**, 291 (2001).
[11] P. Hall and F. T. Smith, J. Fluid Mech. **227**, 641 (1991).
[12] T. M. Schneider, D. Marinc, and B. Eckhardt, J. Fluid Mech. **646**, 441 (2010).
[13] P. Hall and S. Sherwin, J. Fluid Mech. **661**, 178 (2010).
[14] H. M. Blackburn, P. Hall, and S. J. Sherwin, J. Fluid Mech. **726**, R2 (2013).
[15] G. I. Taylor, Phil. Trans. R. Soc. Lond. A **223**, 289 (1923).
[16] J. Wang, J. Gibson, and F. Waleffe, Phys. Rev. Lett. **98**, 204501 (2007).
[17] C. Beaume, in *Proceedings of the Geophysical Fluid Dynamics Program*, edited by Woods Hole Oceanographic Institution (2012) pp. 389–412.
[18] P. G. Drazin and W. H. Reid, *Hydrodynamic Stability* (Cambridge University Press, 1981).
[19] R. M. Clever and F. H. Busse, J. Fluid Mech. **344**, 137 (1997).
[20] F. Waleffe, Phys. Fluids **15**, 1517 (2003).
[21] C. Beaume, E. Knobloch, G. P. Chini, and K. Julien, Fluid Dyn. Res. **47**, 015504 (2015).
[22] V. A. Romanov, Funct. Anal. Appl. **7**, 137 (1973).
[23] P. J. Schmid and D. S. Henningson, *Stability and Transition in Shear Flows*, Applied Mathematical Sciences, Vol. 142 (Springer, Berlin, 2001).
[24] O. Dauchot and F. Daviaud, Phys. Fluids **7**, 335 (1995).
[25] O. Dauchot and F. Daviaud, Phys. Fluids **7**, 901 (1995).
[26] N. Tillmark, Europhys. Lett. **32**, 481 (1995).

[27] P. Manneville, Comput. Fluid Dynamics **18**, 169 (2004).

[28] S. Bottin, F. Daviaud, P. Manneville, and O. Dauchot, Europhys. Lett. **43**, 171 (1998).

[29] A. Prigent, G. Grégoire, H. Chaté, O. Dauchot, and W. van Saarloos, Phys. Rev. Lett. **89**, 014501 (2002).

[30] D. Barkley and L. S. Tuckerman, Phys. Rev. Lett. **94**, 014502 (2005).

[31] V. I. Arnold and L. D. Meshalkin, Usp. Mat. Nauk. **15**, 20 (1960).

[32] L. D. Meshalkin and Y. G. Sinai, J. Applied Mathematics and Mechanics **25**, 1700 (1961).

[33] P. Love, *Bifurcations in Kolmogorov and Taylor-vortex flows*, Ph.D. thesis, California Institute of Technology (1999).

[34] D. Lucas and R. R. Kerswell, J. Fluid Mech. **750**, 518 (2014).

[35] K. Julien and E. Knobloch, J. Math. Phys. **48**, 065405 (2007).

[36] G. P. Chini, K. Julien, and E. Knobloch, Geophys. Astrophys. Fluid Dyn. **103**, 179 (2009).

[37] F. Giannetti and P. Luchini, J. Fluid Mech. **547**, 21 (2006).

[38] J. D. Skufca, J. A. Yorke, and B. Eckhardt, Phys. Rev. Lett. **96**, 174101 (2006).

[39] T. M. Schneider and B. Eckhardt, Chaos **16**, 041103 (2006).

[40] T. M. Schneider, J. F. Gibson, M. Lagha, F. D. Lillo, and B. Eckhardt, Phys. Rev. E **78**, 037301 (2008).

[41] M. Frigo and S. G. Johnson, Proceedings of the IEEE **93**, 216 (2005), special issue on "Program Generation, Optimization, and Platform Adaptation".

[42] V. Mantič-Lugo, C. Arratia, and F. Gallaire, Phys. Rev. Lett. **113**, 084501 (2014).

[43] R. B. Lehoucq, D. C. Sorensen, and C. Yang, "ARPACK Users Guide: Solution of Large Scale Eigenvalue Problems by Implicitly Restarted Arnoldi Methods." (1997).

[44] P. R. Spalart, R. D. Moser, and M. M. Rogers, J. Comp. Phys. **96**, 297 (1991).

[45] L. S. Tuckerman, in *11th International Conference on Numerical Methods in Fluid Dynamics*, Lecture Notes in Physics, Vol. 323, edited by D. Dwoyer, M. Hussaini, and R. Voigt (Springer, Berlin, 1989) pp. 573–577.

[46] C. K. Mamun and L. S. Tuckerman, Phys. Fluids **7**, 80 (1995).

[47] A. Bergeon and E. Knobloch, Phys. Fluids **14**, 3233 (2002).

[48] I. Mercader, O. Batiste, and A. Alonso, Int. J. Numer. Meth. Fluids **52**, 707 (2006).

[49] C. Beaume, A. Bergeon, H.-C. Kao, and E. Knobloch, J. Fluid Mech. **717**, 417 (2013).

[50] J. F. Gibson, *Channelflow: A spectral Navier-Stokes simulator in C++*, Tech. Rep. (U. New Hampshire, 2012) `Channelflow.org`.

[51] Y. Duguet, Private communication (2013).

[52] T. Oppe, W. Joubert, and D. Kincaid, "NSPCG User's Guide: A Package for Solving Large Sparse Linear Systems by Various Iterative Methods," (1988).

[53] J. Jimenez, G. Kawahara, M. P. Simens, M. Nagata, and M. Shiba, Phys. Fluids **17**, 015105 (2005).

[54] J. F. Gibson and E. Brand, J. Fluid Mech. **745**, 25 (2014).

[55] K. Deguchi, P. Hall, and A. Walton, J. Fluid Mech. **721**, 58 (2013).

[56] K. Melnikov, T. Kreilos, and B. Eckhardt, Phys. Rev. E **89**, 043008 (2014).

[57] S. A. Maslowe, Annu. Rev. Fluid Mech. **18**, 405 (1986).

[58] K. Deguchi and P. Hall, J. Fluid Mech. **750**, 99 (2014).

[59] M. Sprague, K. Julien, E. Knobloch, and J. Werne, J. Fluid Mech. **551**, 141 (2006).
[60] K. Julien, E. Knobloch, A. M. Rubio, and G. M. Vasil, Phys. Rev. Lett. **109**, 254503 (2013).
[61] A. M. Rubio, K. Julien, E. Knobloch, and J. B. Weiss, Phys. Rev. Lett. **112**, 144501 (2014).